A two-color magneto-optical trap of Strontium in pursuit of a continuous atomic clock

Dissertation

der Mathematisch-Naturwissenschaftlichen Fakultät

der Eberhard Karls Universität Tübingen

zur Erlangung des Grades eines

Doktors der Naturwissenschaften

(Dr. rer. nat.)

vorgelegt von

Milán János Negyedi

aus Budapest/Ungarn

Tübingen

2025

Gedruckt mit Genehmigung der Mathematisch-Naturwissenschaftlichen Fakultät der Eberhard Karls Universität Tübingen.

Tag der mündlichen Qualifikation:	21.11.2025
Dekan:	Prof. Dr. Thilo Stehle
1. Berichterstatter/-in:	Prof. Dr. József Fortágh
2. Berichterstatter/-in:	Prof. Dr. Christian Groß

Abstract

In this thesis we describe our work on the creation and characterization of a two-color magneto-optical trap suitable for continuous extraction of ultracold Sr atoms. Such a trap would be a very important building block of a continuous atomic frequency standard. With interruption-free evaluation of this standard, the accuracy of neutral atomic clocks could be improved significantly, therefore enabling several important applications.

In this work we will give a brief introduction into the general topic of atomic clocks, and the aforementioned applications in which a continuous clock could provide an improvement. Then we will provide a summary of the relevant theoretical concepts, followed by a detailed discussion of our measurement results. We finish the work with a description of theoretical calculations and their comparison to our measurement data regarding the achievable minimum temperatures in such a trap.

Zusammenfassung

In dieser Arbeit beschreiben wir die Entwicklung und Charakterisierung einer zweifarbigen magneto-optischen Falle, die für die kontinuierliche Extraktion von ultrakalten Sr-Atomen geeignet ist. Eine solche Falle wäre ein sehr wichtiger Baustein für ein kontinuierliches atomares Frequenzstandard. Mit der unterbrechungsfreien Auswertung dieses Standards könnte die Genauigkeit neutraler Atomuhren erheblich verbessert werden, was mehrere wichtige Anwendungen ermöglichen würde.

In der Arbeit geben wir eine kurze Einführung in das allgemeine Thema der Atomuhren und die oben genannten Anwendungen, bei denen eine kontinuierliche Uhr eine Verbesserung darstellen könnte. Anschließend geben wir einen Überblick über die relevanten theoretischen Konzepte, gefolgt von einer detaillierten Diskussion unserer Messergebnisse. Wir schließen die Arbeit mit einer Beschreibung der theoretischen Berechnungen und deren Vergleich mit unseren Messdaten hinsichtlich der erreichbaren Mindesttemperaturen in einer solchen Falle ab.

Contents

"In the beginning, the universe was created. This made a lot of people very angry, and has been widely regarded as a bad move."

Douglas Adams, The Restaurant at the End of the Universe

Chapter 1

Introduction

Ever since the first humans looked up to the sky above them and noticed the repeating patterns of the Sun, the Moon and the stars (nowadays colloquially referred to as day, month and year), keeping time was an important part of life for all of us. Archaeological evidence shows that calendars already existed 5000 years ago in ancient Babylon and Egypt, allowing people to coordinate their social lives and work around them[1]. Later, sundials and water clocks were invented, starting the process of dividing time into ever smaller fragments, a process which continues to our day. It is worth noting that since the oldest times, the measurement of time is based on the measurement of some repetition, either of the same object behaving in a cyclical way, or similar objects behaving reproducibly. As such, the measuring of time always equals measuring frequency. Consequently, the terms time standard and frequency standard will be used interchangeably in this work.

Always inspired by the evolving requirements of society, the next great step in timekeeping came in answer to the needs of both the clergy and the merchants of medieval Europe. The first mechanical clock was installed in 1283 in the Dunstable Priory in England, presumably motivated by the fact that both the aforementioned sundials and water clocks were rendered unreliable or downright unusable by the Northern European weather. An interesting side effect of this invention was the introduction of hours that were each the same length, as this was more convenient to measure with such a clock. In contrast with this, the earlier system had both day and night always consisting of exactly 12 hours, so the day hours were longer during the summer.

In keeping with the logic of advances in timekeeping arriving as answers to the needs of society, the marine chronometer was invented in the middle of the 18^{th} century and perfected by the end of it, answering the 1714 call of the British Parliament for a device that would allow seafarers to determine their longitude while at sea. John Harrison's 1737 invention of the marine chronometer has allowed much more accurate and safe sea navigation for hundreds of years.

Similarly, the expansion of the railroad in Europe and North America made it necessary to synchronize clocks across railway stations. This was accomplished by distributing clock beats over the telegraph network. These beats originated from observatories, culminating in the 1884 establishment of the 24 time zones used today, using the Greenwich Royal Observatory as a zero point and time reference. Marine chronometers of this time were set to so called "time-balls" on towers visible

[1] Historical information in this chapter is based on [1] unless otherwise noted

from the sea, which were dropped at exact predetermined times, a practice later made redundant by introducing the radio broadcasts of hourly signals for the same purpose.

At the beginning of the 1920-s, the Shortt chronometer was invented and was for a short time the most precise time measuring instrument. It used two pendulum clocks linked together, a master clock swinging in vacuum for minimizing disturbances from the environment and the secondary clock linked to it through electromagnetic pulses. This way, the interaction and possible coupling between the two oscillators were also kept at a minimum.

Once again jumping forward, we arrive at 1928, when the potential use of quartz crystals as the core element was discovered at Bell Laboratories. These crystals, cut in a precise shape, had the capability to maintain a constant vibrational frequency when excited by an electric current. Quartz clocks based on this principle enjoyed a brief dominance in precision timekeeping. Brief, because the dawn of the atomic clock was just around the corner. With the proof of concept device (an ammonia maser) created in 1948, and the first caesium clock in 1955, the dominance of using atomic transitions in timekeeping has arrived [1].

It is important to point out that this development did not just represent another jump in the available accuracy of clocks. It also presented the opportunity to decouple the definition of the second from sidereal time (time based on the apparent motion of celestial objects relative to the Earth). While the instability of the rotational period of the Earth was already detected based on measurements with the Shortt clock and quartz clocks [2], they were unsuitable for a global frequency standard, as the quartz clock frequency depends on the crystal shape and manufacturing, and the pendulum clock's period on the pendulum length and a variety of other factors. As such, the discovery of the caesium clock was a welcome opportunity to redefine the second, basing it on a (hopefully) constant physical property, as it happened in 1967 [3]. Indeed, it was already suggested in the 19$^{\text{th}}$ century by Lord Kelvin that the the measurement of "absolute" time should be based on the behaviour of atoms [4]. An important point is that since every other primary SI unit excluding the mole contains the second as part of its definition, almost every conceivable physical measurement is at some point limited by the accuracy of our ability of measuring time [3].

But, as we said in the beginning of this brief history, the (cog)wheel keeps turning, and we are not yet at the limit of what is achievable. A few years later after the 1967 codification of the second, the concept of using optical atomic transitions in contrast to the microwave range frequency used in the Cs clocks was proposed [5]. Such a device would be (and is today) referred to as an *optical atomic clock*. The naive reader might ask, what could be the possible use of further improvements, if the Cs clocks are already only late a second in several million years? In the next section we attempt to provide some applications that served as motivations for such a difficult undertaking.

1.1 Why bother?

It is true that few everyday or commercial applications merit an even higher accuracy standard as a Cs clock. However there are quite a few interesting and important use cases in both industry and research. In the following, we will try to outline

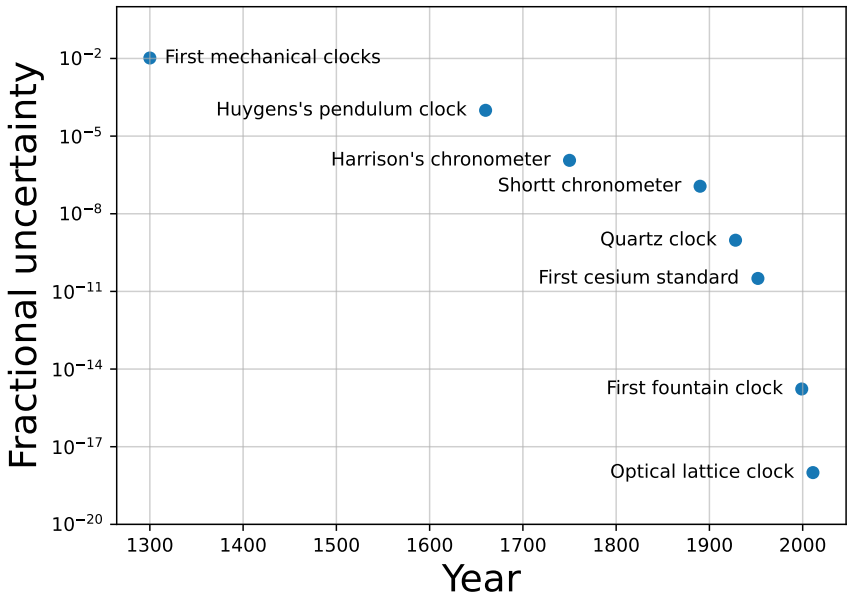

Fig. 1.1: A summary of the history of development of timekeeping devices [1, 2, 6, 7, 8]

some of the areas where using optical atomic clocks with enhanced accuracy and/or precision would prove beneficial.

1.1.1 GNSS systems

Although the acronym GNSS might not be in the public eye, the technology it refers to most certainly is. GNSS stands for *Global Navigational Satellite Systems*, colloquially referred to as GPS. However, GPS (*Global Positioning System*) is only one implementation of a GNSS system by the USA [9]. Similar systems are already deployed and being developed by other countries or groups of countries. Currently, three other system are functional with global coverage; the GLONASS (*Globalnaya Navigazionnaya Sputnikovaya Sistema*, Russia [10]), Galileo (European Union[11]), and Beidou-2 (China [12]). Systems with regional coverage or still under development are the NavIC (*Navigation Indian Constellation*, India) and the QZSS (*Quasi-Zenith Satellite System*, Japan) [13].

These systems are based upon the following technique: Every GNSS satellite is constantly broadcasting its position in very precisely timestamped packets of data, the timestamps of which are being generated by the multiple state-of-the-art caesium atomic clocks on-board [14]. Because of this, the spatial accuracy of the positional data is directly dependent on the frequency stability of said clocks. If a receiver has line-of-sight of at least three satellites (four are preferred for increased accuracy and the determination of elevation), it is possible to calculate the receiver's position without backwards communication from the receiver. At least 24 satellites are required for full global coverage under these requirements.

Standard end-user GPS receivers, such as one would find in a smartphone are already quite well served with the current accuracy of a few meters, however there are a few considerations to make. First, the high interest in the development of

autonomous vehicles will necessitate a higher accuracy on the 10 cm level, without averaging times longer than a few seconds. Since the satellites are supposed to contain the atomic clocks, any system that attempts to improve on the Cs accuracy need to be developed to a technological readiness level suitable for independent space deployment [15]. The DSAC mission flown by NASA also hopes, among other goals detailed in the next part, to improve the GPS system accuracy by a factor of 50 [16].

1.1.2 Deep space navigation

Similar factors need to be considered in a related area where optical atomic clocks could be of great benefit, and that is deep space navigation of spacecraft. Compared to terrestrial navigation, the distances and speeds involved significantly raise the demands on navigational systems. For example a device in a geostationary orbit travels with a velocity of just over $3\,\mathrm{km\,s^{-1}}$. Coverage from the standard GNSS system(s) or dedicated systems such as the *Near Space Network* maintained by NASA seems to be enough for spacecraft navigation within lunar orbit, as they will always see at least the required number of satellites [17, 18, 19]. Navigating lander modules and similar craft on the lunar surface is be more challenging, but the problems are more related to line-of-sight and signal strength rather than frequency accuracy. Outside of lunar orbit, for example Mars exploration missions, the navigation of spacecraft presents different issues [20]. Currently, such craft are tracked using *two-way tracking*, which eliminates the error of the on-board timekeeping of the craft, but makes the necessary infrastructure much more complex. This is the practice because so far there was no demonstrated on-board timekeeping device which would have the required stability for *one-way tracking*, meaning the spacecraft determining its position by comparing the ground based broadcast time with its own internal clock. Optical atomic clocks are a prime candidate for such an improvement, with the aforementioned DSAC mission [16] trying to demonstrate that they can indeed reach the required accuracy.

1.1.3 Chronometric geodesy

The idea behind using atomic clocks for geodesy is rooted in general relativity. Assuming one could measure time accurately enough, the time dilation caused by gravity, and with that the local gravitational potential could be detected. Indeed, the groups of Katori [21] and Ye [22] have already demonstrated gravitational redshift measurement using Sr optical atomic clocks. These techniques, when deployed in a transportable or at least deployable fashion, would have several applications:

- By analyzing the local spatial variations in the gravitational field, it is possible to locate resources deeper underground than it would be with conventional methods [23].
- Monitoring short-scale temporal changes in the local gravity field would allow for the prediction of seismological events like volcano eruptions [23, 24, 25].
- On the longer timescale, the same technique will make it possible to detect slow slip events, which can be responsible for strong earthquakes, thereby allowing earthquake prediction[23, 24].

Additionally, combined with space-based clocks serving to link together their ground-based counterparts, chronometric leveling could also allow the creation of a universal height reference for the Earth as a whole, something inaccessible with today's methods [23, 24].

1.1.4 Very long baseline interferometry

A very interesting technique in radio astronomy is *Very long baseline interferometry (VLBI)*, a prominent example of which is the famous first direct picture taken of a black hole by the Event Horizon Telescope, a group effort based on uniting the results eight radio telescopes [26]. *VLBI* works by correlating the measurements of two or more radio telescopes located far away from each other, the distance between them being the baseline the name refers to. Measurements taken this way are improved by a factor that scales linearly with said baseline. However, it is crucial to have a local oscillator with very low phase noise and very high long-time stability at both telescopes. Low phase noise is needed because the measurement accuracy scales quadratically with it, while the high stability is necessary to keep the coherence between the results of the measurement stations, without which the interference fringes would fade [27]. Each (often remote) observatory having its own optical clock as a reference is not feasible. Thankfully, our globe is already criss-crossed with telecommunication networks using optical fibers, which can be and in fact already were co-opted for scientific applications, such as comparing the accuracies of atomic clocks thousands of kilometers apart [28, 29, 30, 31, 32]. As such, it is a natural idea to keep one highly accurate central clock for *VLBI* measurements, and disseminate its accuracy to each telescope through such a fiber link[33].

1.1.5 Fundamental physics

Last but not least, the Ye group demonstrated a technique where optical atomic clocks can be used to put an upper bound on the inconstancy of the fine-structure constant (α) and the mass of the electron (m_e) [34]. The optical transition frequency in a Sr atomic clock and the frequency of a Hydrogen maser depend differently on α and m_e. By comparing these frequencies through an ultrastable silicon cavity, and monitoring the stability of this ratio in time, changes in the fundamental constants could be detected. Since ultralight bosonic dark matter is predicted to cause oscillations in both constants, the measurement technique also serves as a very sensitive detection system for this type of dark matter. A similar technique was employed by a group at the Yokohama National University, using an Yb lattice clock and a Cs fountain clock to compare the frequency ratios [35]. These systems may also be used to test theories beyond the boundaries of the Standard Model [36, 37].

1.2 Setting standards

Frequency standards are devices which are capable of producing stable and well known frequencies with a given accuracy, and can be further divided into active or passive standards [38]. A passive standard is a physical system with a very well defined and stable frequency response, be it a mechanical or electromagnetic resonator, or a quantum system like an ensemble of atoms or a trapped ion. Such

standards rely on an external *local oscillator*, which is stabilized to the resonance feature exhibited by the standard using a feedback cycle, thereby producing a signal that exhibits the desired accuracy and precision. This technique raises some demanding requirements towards the local oscillator as well, since an unsuitable LO might make it impossible to achieve frequency lock in the first place, for example if it had a too broad intrinsic linewidth compared to the resonance feature, or it might significantly degrade the accuracy of the final signal by proving to have too much noise.

In contrast to passive standards, an active frequency standard is defined based on directly producing a signal with a certain well-determined and stable frequency, such as the ammonia maser mentioned earlier, a spectral lamp (typical examples are neon, argon or krypton), or a He-Ne laser. Currently, there is no active frequency standard accepted by the *BIPM*, the International Bureau of Weights and Measures for a secondary representation of the second. There are, however, several that are accepted as a representation of the metre, among them the aforementioned He-Ne laser [3]. There is also considerable interest towards the realization of superradiant lasers, which would represent an active frequency standard that would be a potential candidate for acceptance as a secondary standard of time [38].

1.2.1 Accuracy and precision

It is at this point that we need to establish the proper definitions of a few terms that will see extensive usage throughout this work. We will use definitions of the BIPM [39]):

- *Accuracy*: The closeness of agreement between a measured quantity value and a true quantity value of a measurand;[2]
- *Precision*: The closeness of agreement between indications or measured quantity values obtained by replicate measurements on the same or similar objects under specified conditions (analogous to repeatability)[2];
- *Stability*: A property of a measuring instrument, whereby its metrological properties remain constant in time;
- *Uncertainty*: non-negative parameter characterizing the dispersion of the quantity values being attributed to a measurand, based on the information used.

When comparing the performance of clocks, it is useful to introduce *relative* or *fractional* quantities, where the corresponding *absolute* quantities are divided by the center frequency of the reference.

If we denote the frequency of the local oscillator with f_{LO}, the transition frequency of the system with f_c and the atomic transition frequency with f_0 [3], we can write the fractional frequency difference as:

$$y \equiv \frac{f_c - f_{LO}}{f_0} \tag{1.1}$$

[2]It is important to note that according to these definitions, accuracy and precision are not quantities, only qualitative descriptors. As such, they should not be assigned a numerical value.

[3]The two are not necessarily equal because of possible systemic shifts in the measurement.

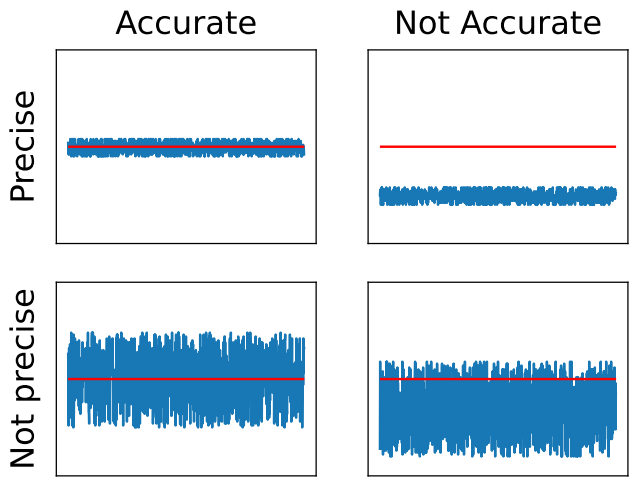

Fig. 1.2: An illustration of the difference between precision and accuracy

When measured, the continuous signal $y(t)$ will be reduced to a series of discrete values averaged over the measurement time τ:

$$\bar{y}_i = \frac{1}{\tau}\int_{t_i}^{t_i+\tau} y(t)dt \tag{1.2}$$

called the normalised frequency deviation. These measurement points will form a series characterized by the result of some statistical process, and their values will fluctuate. The mean value and the square standard deviation of a measurement series are defined as:

$$\bar{y} = \frac{1}{N}\sum_{i=1}^{N} y_i \tag{1.3}$$

and

$$s_y^2 = \frac{1}{N-1}\sum_{i=1}^{2} N(y_i - \bar{y})^2 \tag{1.4}$$

It is important to note that the mean value and standard deviation of the fluctuation are not the same as the mean value and standard deviation of the underlying *statistical process*. Assuming stationarity for the process, according to the central limit theorem its distribution function will asymptotically approach a Gaussian distribution as T goes to ∞. Then we would write:

$$p(y) = \frac{1}{\sigma\sqrt{2\pi}}\, exp\left(-\frac{(y-\bar{y})^2}{2\sigma^2}\right) \tag{1.5}$$

Now the properties of the distribution can be written as:

$$\langle y\rangle = \int_{-\infty}^{\infty} yp(y)dy \tag{1.6}$$

and

$$\sigma^2 = \int_{-\infty}^{\infty} (y - \langle y\rangle)^2 p(y)dy \tag{1.7}$$

From these definitions we can see that the properties of the process do not equal those of the measurement series, and would only be the same for an infinitely long measurement. With finite time, $\langle y \rangle$ and σ^2 can only be estimated from $\bar{y}$ and s_y^2, and even then only for a stationary process. Stationarity however is not guaranteed when working with a frequency standard. There are different sources of disturbances and drifts affecting the system, many of them capable of introducing long-term drifts into the results.

Such drifts mean that the quantities in our measurement are not independent from each other, but in fact correlated by the underlying effect causing the drift. This results in standard deviations calculated for differently sized time segments of the measurement showing different results, the estimation of the properties of the underlying statistic process would not be possible in this case[38].

Therefore, a new metric was needed to characterize frequency standards in general and atomic clocks in particular. The generally accepted method used today was proposed in 1966 by Dave Allan [40] and is referred to as Allan variance. For the sake of completeness, we note that this new measure is a specific case of a more general technique called M-sample variance (originally termed "N-sample variance")[4].

The general M-sample variance is defined as:

$$\sigma^2(M,T,\tau) = \frac{1}{(M-1)} \sum_{i=1}^{M} \left(\bar{y}_i^2 - \frac{1}{M} \left[\sum_{i=1}^{M} \bar{y}_i \right]^2 \right) \tag{1.8}$$

where τ is the measurement time of a sample, T is time between measurements and M is the number of samples.

Taking the specific case of the Allan variance as used today means we set $M = 2$ and $T = \tau$:

$$\sigma_y^2(2,\tau,\tau) = \sigma_y^2(\tau) = \left\langle \sum_{i=1}^{2} \left(\bar{y}_i - \frac{1}{2} \sum_{j=1}^{2} \bar{y}_j \right)^2 \right\rangle = \frac{1}{2} \left\langle (\bar{y}_2 - \bar{y}_1)^2 \right\rangle . \tag{1.9}$$

Essentially, this means that the Allan variance for a given τ gives the expected frequency difference between measurement points separated by τ seconds. The Allan deviation is also often defined, analogously to the standard deviation:

$$\sigma_y(\tau) = \sqrt{\sigma_y^2(\tau)} \tag{1.10}$$

When analysing the Allan deviation of an oscillator, one will often get a result similar to the idealized plot pictured in Fig. 1.3:

As we can see in Fig. 1.3, different types of noise having different power law dependencies result in them being identifiable in the Allan deviation plot. A typical example is the $\tau^{-0.5}$ dependency of the white noise. The aforementioned correlated processes show up as the so-called "flicker floor" in the middle of our plot with a constant τ dependence, or as the processes with positive slope, corresponding to a random walk ($\tau^{0.5}$) or a (linear) drift (τ^1). Analysing the Allan deviation plot will offer several useful insights, such as at what point further time averaging stops being useful, and if measured long enough, also offers a hint on the types of noise

[4] in this work, we use the notation and derivation of the M-sample and Allan variance based on frequency variation instead of phase variation as in the original proposal, as seen in [38]

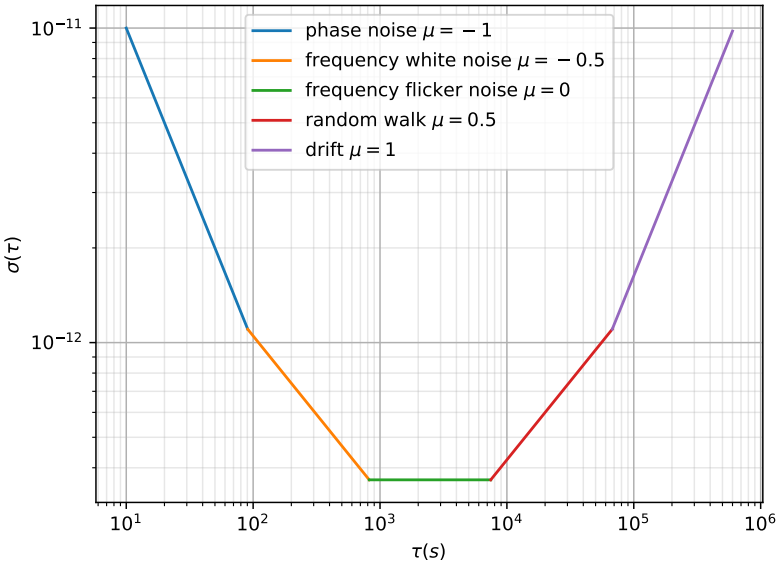

Fig. 1.3: A theoretical illustration of various types of noises and their measurement time dependency in an Allan deviation plot

processes present in the system, often making it possible to identify and eliminate their sources. The latter usage is not restricted to clocks, stabilized lasers used for other purposes are also often analysed in this manner.

Having established our method of evaluating and comparing clock performance, let us put it to good use, and take a look at some of the atomic clocks relevant to our discussion.

1.2.2 Traditional atomic clocks

In the standard caesium atomic clock, an oven emits a beam of caesium atoms at a temperature of a few hundred Kelvins. These atoms are selected using a magnetic filter to be in a specific state (the $F = 3$ lower clock state), and fed into a microwave resonator cavity, that changes the state of the atoms with an efficiency dependent on the radiation introduced into the cavity at the same time. After exiting the cavity the atoms are once again filtered for the concurrent state (the $F = 4$ upper clock state), and their flux is detected. The frequency of the radiation provided by the local oscillator is stabilized to this resonance feature. According to the definition of the *BIPM* [3], this transition has a frequency of $f = 9.192\,631\,770\,\mathrm{GHz}$, which can then be converted to the ubiquitous 10 MHz "lab reference" signal, or a one pulse per second reference signal. Such a system is suitable to achieve a fractional uncertainty of 10^{-14} [41]. When considering such a caesium clock, the Allan variance can be related to instrumental parameters using the following equation [41]:

$$\sigma_y(t) = \frac{\eta}{2\pi}\frac{\delta\nu}{\nu}\frac{1}{\mathrm{SNR}}\sqrt{\frac{1}{\tau}} \tag{1.11}$$

where η is a numerical factor depending on the lineshape of the resonance, $\delta\nu$ is the measured linewidth of the transition, ν is the fundamental transition frequency

and SNR is the signal-to-noise ratio of the measurement of the spectral feature.

This equation suggests a few ways of improving the quality of the clock:

- Decrease the measurement linewidth: In a usual system the caesium atoms have a temperature of about 400 K, which causes a significant Doppler broadening. By laser cooling the atoms before the measurement, this broadening can be eliminated, significantly improving the results. However, this technique encounters a fundamental limitation in the natural linewidth of the transition;
- Improve the SNR: as we will discuss later, the SNR can be improved, but it will hit a point of diminishing returns because technological and even quantum-mechanical limitations will have stronger and stronger effects;
- Integrate longer: Choosing longer and longer integration times will improve the measurement uncertainty, however, for many applications integration times longer than a day are not feasible.

Utilizing many of these techniques mentioned above, the peak performance of the caesium atomic clock currently stands at a fractional uncertainty of $\approx 10^{-16}$ [42] after a day of averaging. The reader will notice that we have left out a parameter that can be subject to optimization: raising ν. This is equivalent to a complete change in the system, since the fundamental transition frequency is determined by the atomic species used which is exactly the core idea behind the optical atomic clocks, as it will be detailed in the next section.

1.2.3 Optical atomic clocks

A few years after the second was officially redefined based on the caesium clock, the idea to use atomic transitions with frequencies in the optical regime rather than the microwave was already proposed [5]. Choosing a transition frequency higher by about 5 orders of magnitude allows optical clocks to surpass the accuracy of the best performing microwave clocks, or conversely, allows much shorter integration times for achieving the same accuracy. As some tasks are clearly not feasible with the one day integration time usual for Cs clocks, such as providing timestamps for the aforementioned GNSS navigation, a reduction of the averaging time is a development worth pursuing.

We differentiate between two main types of atomic clocks based on the net electrical charge of the atom(s) used in the system: ion clocks and neutral atom clocks.

Ion clocks

In an ion clock, a single ion of a given species is captured in a quadrupole trap in ultra-high vacuum [43]. This ion is cooled to a kinetic energy equivalent to a few mK, which localizes it to a few tens of nanometres in the centre of the trap. For a neutral atomic clock this "temperature" would provide far too much Doppler broadening to be useful for any kind of precision spectroscopy, however, the strong trapping potential localizes the ion enough to be in the Lamb-Dicke regime. This means the average oscillation amplitude of the ion is small enough compared to the wavelength of the probe light, that first order Doppler broadening is suppressed because of the quantized nature of vibrational states in the trap [5].

Single ions can have trap lifetimes in excess of a month, since they can be almost perfectly isolated from the environment, and because the Coulomb interaction allows much tighter confinement compared to neutral atom clocks. After this, the ion can be interrogated with an ultrastable laser as a local oscillator. The best performing ion clocks currently can provide the same time stability in about a hundred seconds as the caesium fountain clocks can in a day (10^{-16}). Six of the eleven current secondary time standards as recognized by the BIPM are ion clocks. These are ([3], [43]):

- $^{27}Al^+$ ion, using the $3s^2\ ^1S_0 - 3s3p\ ^3P_0$ transition.

  This ion cannot be cooled directly, only with a buffer ion, which significantly increases the complexity of the system. Additionally, many of the required lasers lie in the uncomfortable wavelength range of below 350 nm, including the clock transition at 267 nm.

- $^{199}Hg^+$ ion, using the $5d^{10}6s\ ^2S_{1/2} - 5d^9 6s^2\ ^2D_{5/2}$ transition.

  The species chosen for the DSAC (Deep Space Atomic Clock) mission of NASA [16]. With a clock transition at 282 nm, and multiple other lasers below even 200 nm, the laser instrumentation of this clock system is very challenging.

- $^{171}Yb^+$ ion, using the $6s\ ^2S_{1/2} - 5d\ ^2D_{3/2}$ transition (quadrupole)

  Currently unique amongst ionic species, $^{171}Yb^+$ has two transitions suitable for interrogation at atomic clock accuracy levels. The quadrupole transition offers a "broader" natural linewidth at the subhertz level, offering lower light shifts in return.

- $^{171}Yb^+$ ion, using the $6s\ ^2S_{1/2} - 4f^{13}6s^2\ ^2F_{7/2}$ transition (octupole)

  The octupole transition of $^{171}Yb^+$ has an astonishing nanohertz order of magnitude linewidth, but suffers from significantly higher light shifts.

- $^{40}Ca^+$ ion using the $4s\ ^2S_{1/2} - 3d\ ^2D_{5/2}$ transition

  The lack of hyperfine structure in the $^{40}Ca^+$ ion allows for comparatively simple cooling setups.

- $^{88}Sr^+$ ion using the $5s\ ^2S_{1/2} - 4d\ ^2D_{5/2}$ transition

  Similarly to $^{40}Ca^+$, $^{88}Sr^+$ has a convenient structure for cooling with no hyperfine structure and wavelengths accessible by standard diode lasers.

Ion clocks typically only trap one ion to interrogate, since multiple ions in a trap would interact strongly, shifting the transition frequency uncontrollably. Using one particle for the measurement means that the uncertainty of ion clocks is ultimately limited by *Quantum Projection Noise (QPN)* [44]. Essentially, the *QPN* limit results from the fact that the interrogated ion (or as we see later, any particle) will always be prepared in a state that is a mixture of (at least) the two states of the clock transition, that is to say: $|\Psi\rangle = c_A|A\rangle + c_B|B\rangle$. c_A and c_B might change depending on parameters of the experiment, but neither will equal zero or one. This can be thought of as randomly projecting the state vector onto one of the two clock states. The statistical nature of this projection will introduce a noise term into the result of the measurement, which is quite hard to counter.

For typical measurement parameters (about 120 ms for a measurement cycle), *QPN* means an uncertainty of $3 \cdot 10^{-15}/\sqrt{\tau}$. In contrast to this, a few thousand neutral atoms can be interrogated at the same time without them interacting with the same interaction strength as ions would, thereby making it possible to lower the *QPN* limit on the noise.

Neutral atom optical clock

The operation of a neutral atom optical clock starts with a hot beam of atoms from an oven [43]. Using precisely tailored magnetic fields and stabilized lasers, the atoms in the beam can be slowed and captured in a *Magneto-optical Trap (MOT)*. We will discuss the theoretical and practical considerations behind these techniques in Section 2.2. For our current topic the only relevant part is that all current neutral atomic clocks use cooling schemes that require at least two cooling transitions, which cannot all happen at the same place at the same time.

The following atomic species are currently accepted as a secondary representation of the second by the BIPM:

- ^{199}Hg atom on the $6s^2\ {}^1S_0 - 6s6p\ {}^3P_0$

  Similar to the ionic Hg clock, the cooling and clock wavelengths of the Hg neutral clock are technologically challenging, lying in the deep UV region.

- ^{87}Sr atom on the $5s^2\ {}^1S_0 - 5s5p\ {}^3P_0$

  Strontium offers two isotopes for neutral atomic clocks. The fermionic 87 isotope has naturally occurring state mixing opening the clock transition, making it unnecessary to use magnetic fields to do the same, as in the case of the 88.

- ^{88}Sr atom on the $5s^2\ {}^1S_0 - 5s5p\ {}^3P_0$

  The bosonic 88 isotope has no hyperfine structure in contrast to the 87, making the cooling and interrogating setups significantly simpler.

- ^{171}Yb atom on the $6s^2\ {}^1S_0 - 6s6p\ {}^3P_0$

  Ytterbium lattice clocks have recently received attention regarding using multiple clock transitions in the same system to aid the search for dark matter and possibly find physics beyond the Standard model [36, 37]

For the sake of completeness, we mention the last accepted secondary standard, which is a microwave frequency clock utilizing rubidium.

Using the atomic cloud resulting from a MOT as frequency standard was limited at first by the fact that free-space interrogation would have severely limited interrogation times, and introduce other error sources like inhomogeneities in the Gaussian profile of the probe laser, whereas localizing them in a conservative optical potential (an optical dipole trap or lattice) would have caused significant and uncontrollable Stark shifts on the transition.

The solution to this problem came with the concept of the "magic wavelength", a wavelength where the differential Stark shift becomes zero for a given transition, in our case the clock transition [45]. Operating the trapping laser at this frequency means that the light shifts on the clock transition states resulting from the comparatively high intensities of the trapping laser will cancel each other out. However,

practically achievable optical trap depths still mean that the two step cooling is necessary, as atoms cooled only by the first step would have too much remaining energy to be captured in the trap. The fact that several hundred thousands to a few millions of particles are interrogated in contrast to the single ion in the ion clock result in a very significant decrease in the *QPN*, the Allan deviation limit of which scales with the inverse square root of the number of particles.

Removing the constraint of the quantum projection noise does not, in itself, make neutral atom clocks automatically superior to ion clocks. There is another very significant issue hampering the performance of optical atomic clocks (the effect is also present in ion clocks, but there the *QPN* remains the dominating factor), and that stems from their cyclical nature. To explain this, let us take a look one more time at equation of the Allan deviation for a neutral atomic clock:

$$\sigma_y(t) = \frac{\eta}{2\pi}\frac{\delta\nu}{\nu}\frac{1}{\mathrm{SNR}}\sqrt{\frac{T_c}{\tau}} \tag{1.12}$$

There is a new term in the equation for the Allan deviation, the cycling time T_c. As we will detail in the second chapter, a significant portion of the operational time of every optical atomic clock is spent preparing the sample in the correct motional and atomic state before interrogation can begin. As this time will not contribute to lowering the measurement error, it is essentially wasted. Indeed, in most systems the actual interrogation time is actually less than half of the total measurement time.

There is another, even more serious issue directly impacting clock performance. This problem was first described in 1987 by J. G. Dick [46]. The cycling nature of the clock results in the sampling of the measured clock frequency with the cycling frequency. This converts the high-frequency noise of the local oscillator into low-frequency noise, which negatively impacts the long-term performance of the clock. The Dick effect results in an uncertainty limit of $10^{-15}/\sqrt{\tau}$ for the clocks, even though the number of particles reduces the previously dominating noise factor, the *QPN* to the order of magnitude of 10^{-18}.

The first logical solution to this problem is lowering the noise of the local oscillator after all, if there is no high-frequency noise to be downconverted, the issue is mitigated. Unfortunately, the current best laser stabilization schemes do not offer a reduction down to the QPN limit. These schemes rely on stabilizing the lasers to extremely stable optical cavities that are utilizing cryogenic cooling and/or special crystalline or metamaterial mirrors [47, 48]. While a viable route of improving atomic clock performance, engineering the local oscillator as close to perfection as possible is not the only, and perhaps also not the most straightforward way of handling the issue.

Other alternative solutions are:

- optimizing the cooling cycles to decrease the ratio of dead time to useful measurement time [49];
- utilizing two atomic ensembles and locking the clock laser to the one currently not in a preparation cycle [50];
- using non-destructive spectroscopy to reuse the atoms [51];

These approaches are similar in that they still try to circumvent the problem resulting of cyclical measurement instead of eliminating it by providing a continuous supply of atoms to interrogate. One can try separating the two cooling cycles in space instead of time, and transfer the atoms in some way between the two locations [52]. While this approach is promising, it has the issue of requiring a lot higher vacuum chamber volume, as the two cooling cycles need to be optically blocked from each other. If this is not done, the scattered photons from the broad line cooling cycle will heat up the atoms supposedly taking part in the narrowline cooling cycle as it can be seen from previous attempts [53, 54]. As it is outlined in Section 1.1, many of the possible future application require an optical atomic clock to be transportable, especially those that are space-related, where every cubic centimeter and every gram is at a premium. In such applications, the necessarily increased volume and weight of the above technique would be a serious drawback, therefore in the current work we will consider an alternative solution to the issue.

Said alternative solution to the spatial separation is to choose a different cooling setup as commonly used, with the two cooling cycles not sharing a common ground state. This will be our chosen solution to attempt creating a continuous source of cold atoms to interrogate. We will detail the usual setup, and our modifications to it in Section 2.2.

"It's still magic even if you know how it's done."

Terry Pratchett, A Hat Full of Sky

Chapter 2

Tools of the trade

In this chapter, we will provide a brief summary of the most relevant theoretical concepts and techniques necessary to provide a sample of cold atoms, such as Doppler and sub-Doppler laser cooling, atomic state manipulation, and atomic confinement in optical or magnetic potentials. Our notation and general process of thought follows that of [55], unless noted otherwise. We will also discuss those properties of the Sr atom and its 88 isotope that are relevant for the laser cooling and interrogation processes. First we give a general summary in Section 2.1 and then go into detail in later sections where necessary.

2.1 Laser cooling

Basic concepts

The idea of slowing neutral atomic gases by means of laser radiation was already proposed in [56] less than two decades after the very first laser was demonstrated in 1960 [57]. This process was only hastened along with more and more wavelengths being accessible with diode lasers.

First we consider a two level atom in free space, with energy levels E_g for the ground state and E_e for the excited state, the transition between them having a frequency $\nu_{tr} = \omega_{tr}/2\pi$ and a natural linewidth γ. Should this atom encounter a well-collimated beam of coherent light characterized by wave vector $\vec{k}$, it will start absorbing photons from it. Due to conservation of momentum, after the absorption the momentum previously held by the photon is transferred to the atom. This will change the momentum of the atom from $p_1 = m\boldsymbol{v}_1$ to $p_2 = m\boldsymbol{v}_1 + \hbar\boldsymbol{k} = m\boldsymbol{v}_2$. In the case where the atom and the absorbed photon were counterpropagating, v_2 is smaller than v_1, the atom lost speed. Momentum changes during spontaneous emission on the other hand, will average out over many absorption-emission cycles because of the spatial symmetry of the process. This results in an average light force acting on the atom. The randomness of this process also presents a lower limit to the achievable temperatures with this type of laser cooling, as we will see in Subs. 2.1.1.

To calculate this force, we need to first introduce the scattering rate:

$$\Gamma_s \equiv \frac{1}{2}\frac{s_0}{1 + s_0 + (2(\delta - \boldsymbol{k}\boldsymbol{v})/\gamma)^2}\gamma,$$

with $s_0 = I/I_s$ the on-resonance saturation parameter and $I_s = \pi hc/3\lambda^3\tau$, $-\boldsymbol{k}\cdot\boldsymbol{v}$ the Doppler shift. Additionally, $\delta = \omega_{tr} - \omega_L$ is the detuning, where ω_L is the angular

frequency of the excitation laser. The average force acting on the atoms is then:

$$\boldsymbol{F} = \hbar \boldsymbol{k} \Gamma_s = \frac{\hbar \boldsymbol{k}}{2} \frac{\gamma s_0}{1 + s_0 + (2(\delta - \boldsymbol{kv})/\gamma)^2}, \tag{2.1}$$

since the collimation of the beam means each absorbed photon imparted momentum on the atom in the same direction. It can be seen that this expression saturates in the limit of high intensity, resulting in a maximum force $F_{max} = \hbar k \gamma / 2$ possible on the atoms.

2.1.1 Precooling and capture

The velocity change will result in a change in the Doppler shift, and without further measures, the atoms will be slowed only until the changed shift takes them out of the range determined by the greater of either the transition linewidth or the laser linewidth. Diode lasers used for cooling typically have linewidths of a few MHz, and sometimes much below that. This means in almost all cases the factor determining this "natural" capture velocity of the transition is the natural linewidth $v_{nc} = \gamma/k$. For example, the blue transition in Sr has a linewidth of $\gamma/2\pi = 32\,\mathrm{MHz}$, resulting in $\mathrm{v_{nc}} = 14.8\,\mathrm{m\,s^{-1}}$. From a thermal beam, typically with a temperature around 500 K this would capture only a minuscule fraction of the total atom flux (around $1{*}10^{-10}$). For some experiments, this is enough, especially for atoms with a lower evaporation temperature such as rubidium, where capturing atoms directly from a dispenser is an established practice [58]. As we will show later in this work, direct loading of Sr is also possible, but it will unavoidably result in significantly lower equilibrium atom numbers in the system than what is achievable using other methods, at least for the first stage MOT.

One method to involve more thermal atoms in the cooling process is to increase the cooling laser linewidth to a significantly higher value than that of the natural linewidth [59]. Typically one would need to increase the laser linewidth to about a 100γ to match the efficiency achievable with other methods described below (by being close to saturation in the whole frequency range). In the case of strontium, a typical laser used for cooling on the blue transition has a linewidth of a few MHz-s, meaning that it would need to be broadened by a factor of thousand to provide a suitable range of addressed velocities. This also means a required increase of the total laser power by the same factor, which, if even possible, makes it necessary to use additional components such as a tapered amplifier.

An alternative of this technique is to simply sweep the laser frequency instead of increasing the linewidth (merely a difference of the timescale of the frequency modulation). In this case, the cooling laser intensity does not need to be increased, and with the proper timing, slowed packets of atoms will be created [60]. However, this way no continuous beam of slowed atoms is produced, which might be detrimental to some experiments.

Yet another method is to create a tailored energy level shift along the path the atomic beam travels. This can be a static magnetic or electric field, producing the required shift during the Zeeman or Stark effect, respectively. These devices are called *Zeeman slowers* [61] or *Stark slowers* [62]. With a correctly tailored field profile, atoms will stay in resonance with the cooling beam while traveling, allowing the cooling of a significant number of atoms, only limited through the length of the device.

For the magnetic case, there is a requirement for the ground and excited state to have a nonzero differential shift. If this holds, the optimal profile is given by:

$$B(z) = B_0\sqrt{1 - z/z_0},$$

with $z_0 \equiv Mv_0^2/\eta\hbar k\gamma$, $B_0 = \hbar k v_0/((g_e M_e - g_g M_g)\mu_B)$. The indices g and e denote ground and excited state, respectively, g is the Landé g-factor, and M is the magnetic quantum number. The design factor $\eta < 1$ corresponds to the allowed length of the cooler, with $\eta = 1$ corresponding to maximum achievable deceleration (and therefore minimum length). The effective frequency detuning in this case is given by:

$$\Delta = \frac{2(\delta - \boldsymbol{k}\cdot\boldsymbol{v}(z) + \mu\cdot B(z)/\hbar)}{\gamma},$$

where z is the coordinate along the axis of the field, and $\mu = (g_e M_e - g_g M_g)\mu_B$. This field is traditionally created by a tapered solenoid, although permanent magnets are also seeing more and more use[63].

The electric case is more impractical for cooling atoms, as it requires broad transition linewidth in the 10 MHz order of magnitude to create adequate deceleration. However, it is used in molecule cooling experiments.

2.1.2 Optical molasses and Magneto-optical Trap

Optical molasses

For cooling the atoms further, a 6-beam arrangement is usually used, three pairs counterpropagating orthogonal to each other. In the following, we will study the 1D case of a single beam pair, as the important results obtained there generalize pretty well to the 3D case. Atoms moving with a nonzero velocity in the region of the overlap will experience a velocity-dependent force. If the laser frequency is tuned below resonance, the direction of the force will be opposite to the atomic velocity, slowing the atoms independent of the direction of their movement. Assuming a low intensity case, the contributions of the two beams to the net force can be directly summed up:

$$\boldsymbol{F}_{OM} = \frac{\hbar\boldsymbol{k}\gamma}{2}\left(\frac{s_0}{1 + s_0 + [2(\delta - \boldsymbol{k}\cdot\boldsymbol{v})/\gamma]^2} - \frac{s_0}{1 + s_0 + [2(\delta + \boldsymbol{k}\cdot\boldsymbol{v})/\gamma]^2}\right). \tag{2.2}$$

Neglecting terms of order $(kv/\gamma)^4$, Eq. (2.2) simplifies to:

$$\boldsymbol{F}_{OM} = \frac{8\hbar k^2\delta s_0\boldsymbol{v}}{\gamma(1 + s_0 + (2\delta/\gamma)^2)^2} \equiv -\beta\boldsymbol{v}. \tag{2.3}$$

For a red-detuned laser (a positive δ value), β will also be positive, the force will decelerate the atoms. The force described by Eq. (2.3) is similar to that acting on an object moving in a viscous medium, therefore this arrangement is called an *Optical Molasses (OM)*. To find the limit of this cooling process, we need to consider that the atomic kinetic energy changes in discrete steps also with each $\Delta p = \hbar k$ momentum exchange, $\Delta E = \hbar^2 k^2/2M \equiv E_r$, the *recoil energy*, with M the mass of the atom.

In a single scattering event in the cooling process the atom absorbs and then emits a photon. The absorbed photon on average had an energy of $E_{abs} = E_{tr} + E_r$,

with E_{tr} the energy difference between the ground and excited state of the atom. In the same way, the energy of the emitted photon is $E_{em} = E_{tr} - E_r$. The difference in the energy, $\Delta E = E_{abs} - E_{em} = 2E_r$ is lost from the light field, and manifests as a heating process that works against the cooling. The scattering events occur with a rate of $2\Gamma_s$ because there are two beams participating. As such, the heating rate is $4E_r\Gamma_s$.

In the steady state the contributions of the two processes are equal, so we get the limit of this cooling by setting $4E_r\Gamma_s = \boldsymbol{F} \cdot \boldsymbol{v}$. This results in

$$T_D = \frac{\hbar\gamma}{8}\left(\frac{2\delta}{\gamma} + \frac{2\gamma}{\delta}\right)$$

for the equilibrium temperature (the *Doppler cooling limit*). This result has a minimum at $\delta = \gamma/2$. Usually however, MOT-s are not operated at this detuning for reasons related to atom capture efficiency, typical detunings are in the range of $1.5...2\gamma$.

Sub-Doppler cooling

For specific polarization configurations, there are additional cooling effects resulting in temperatures lower than T_D. These configurations are collectively termed sub-Doppler cooling, even though the underlying effects being different. The most well-known from these is the so-called Sisyphus cooling, which is created by counterpropagating beams of orthogonal linear polarization. These create a standing wave field where the polarization of the field goes from linear (at 45 degrees between the two original) to positive circular to linear (orthogonal to the previous one) to negative circular, and so on. At a given point, the electric field of the light shifts the atomic energy levels of the separate magnetic states of the ground state by

$$\Delta E_g = \frac{\hbar\delta s_0 C_{ge}^2}{1 + (2\delta/\gamma)^2},$$

C_{ge} being the Clebsch-Gordan coefficients of the different magnetic ground substates. C_{ge} depends on the polarization of the light field and the magnetic substate the atom is in.

For the simplest case (where this cooling process is possible) of an $J_g = 1/2$ to $J_e = 3/2$ transition, this results in two potential landscapes of sinusoidal "hills and valleys", shifted by $\lambda/4$ for $M_J = +1/2$ and $M_J = -1/2$. Atoms propagating in these landscapes "climb" the potential hills, losing from their kinetic energy, and at the maximum of the potential getting pumped to the other magnetic substate which has a potential minimum at that point, thereby restarting the climb (hence the name of this cooling process relating it to the ancient Greek myth of Sisyphus being forced to roll a boulder up a mountain for eternity). We can see that the efficiency of this cooling is velocity-dependent, with the optimum being the velocity that results in the atoms moving $\lambda/4$ distance between two scattering events. Essentially this results in Sisyphus cooling addressing only given velocity classes in an ensemble, in contrast to Doppler cooling, which works on all velocity classes at the same time.

Another sub-Doppler cooling configuration, one of particular importance to us is the σ^+ - σ^- configuration consisting of two (or six) counterpropagating beams with orthogonal circular polarization. In Chapter 4 we will investigate the details of this

cooling process, for now we only remark that the required polarizations being the same as that of a magneto-optical trap means that for certain cooling transitions (having at least J=1 in the ground state) it is possible to have the effect occur during the operation of the MOT, meaning that it is suitable for continous cold atom generation (in contrast to a lin/lin configuration which provides no trapping force on its own).

Magneto-optical trap

Looking at Eq. (2.3), we can see that it only has a velocity-dependent term, only slowing the atoms but not restricting them in space. Spatial confinement is added to a molasses by adding a magnetic field to the system. This arrangement is called a *magneto-optical trap*. Specifically, a quadrupole field, usually generated by two coils in an anti-Helmholtz configuration. Such a field is described (around the minimum point of the field) by the equation $B = G\sqrt{r^2 + 4z^2}$ with $r^2 = x^2 + y^2$ and G the magnetic field gradient, which is constant in the region where the atom-light interactions happen.

If this field is overlapped with an optical molasses created by six orthogonal beams, pairwise σ^+ and σ^- polarized (with the σ^- beam coming in from the directions where the magnetic potential is increasing for positive $M_{J,e}$-s), then atoms away from the center of the field will experience a position-dependent detuning, which will result in them interacting preferentially with the beam coming in from the same side of the trap that the atoms are, thereby creating a restoring force. This arrangement works on all transitions with $\Delta J = 1$.

To describe the compound effect of the quadrupole field and the circularly polarized beams on our atoms, let us once again take a look at Eq. (2.2), but this time we shall include the Zeeman shift caused by the magnetic field in our effective detuning:

$$\boldsymbol{F}_{MOT} = \frac{\hbar \boldsymbol{k} \gamma}{2} \left(\frac{s_0}{1 + s_0 + [2(\delta - \boldsymbol{k} \cdot \boldsymbol{v} + \mu' B/\hbar)/\gamma]^2} - \frac{s_0}{1 + s_0 + [2(\delta + \boldsymbol{k} \cdot \boldsymbol{v} - \mu' B/\hbar)/\gamma]^2} \right), \quad (2.4)$$

where $\mu' \equiv (g_e m_{F,e} - g_g m_{F,g})$. Once again neglecting terms of fourth order and higher in the effective detuning, the force becomes:

$$\boldsymbol{F}_{MOT} = -\beta \boldsymbol{v} - \kappa \boldsymbol{r}, \quad (2.5)$$

where $\kappa = \frac{\mu' G}{\hbar k} \beta$.

Applying such a force to the atoms will result in a (strongly) damped oscillation. As such, the MOT slows the atoms and localizes them to the center of the field.

2.2 The strontium atom

Let us now take a closer look on our chosen atomic species, the second component of the ligh-matter interaction, strontium. Strontium is an alkali-earth metal with an electron structure of [Kr]$5s^2$. The two-electron outer shell gives rise to a broad

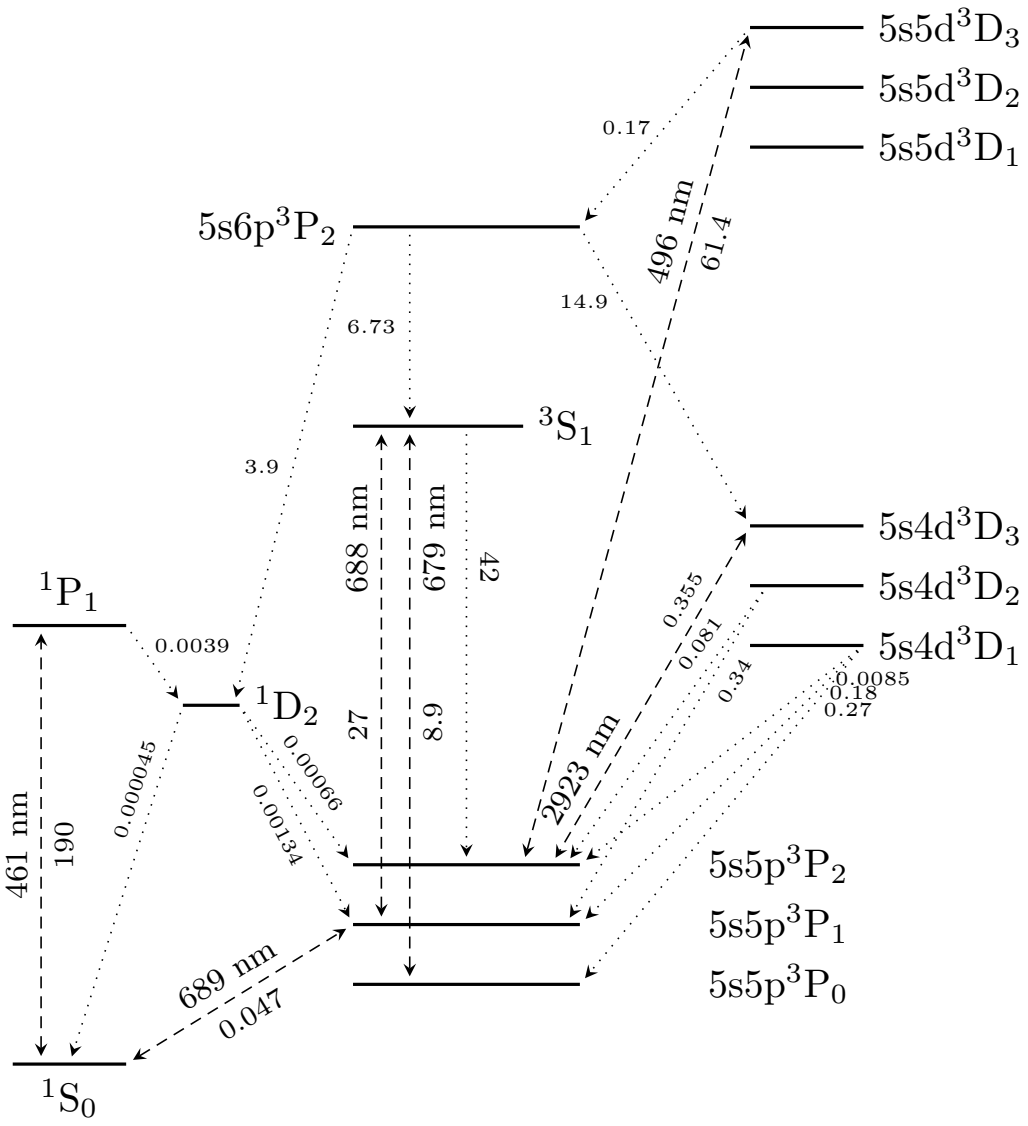

Fig. 2.1: A partial diagram of the energy levels and transitions of strontium. Decay rates are denoted in units of 2πMHz.

range of singlet and triplet states, offering transitions from broad to ultranarrow for many possible cooling and spectroscopy techniques, as we can see in Fig. 2.2.

The ground state has a configuration of $5s^2\,{}^1S_0$. There exists a strong, dipole allowed transition to $5s5p\,{}^1P_1$, commonly called the *blue* cooling transition. The rest of the depicted and currently relevant energy levels have a triplet configuration, and are accessible only through a few specific channels from the aforementioned two states, because of the dipole selection rule $\Delta S = 0$.

The first possibility of crossing between the two groups of states is spontaneous decay from the $5s5p\,{}^1P_1$ through the $5s4d\,{}^1D_2$ to the $5s5p\,{}^3P_J$ triplet. Especially important for us here is that this decay channel populates the metastable $5s5p\,{}^3P_2$ state. The control of this level's population is essential to the optimal operation of all types of Sr MOT-s, either because of it being a dark state accumulating atoms, in which case minimizing the population is the desired goal, or because $5s5p\,{}^3P_2$ is the ground state of the second cooling stage, and maximizing its population is crucial

in that case.

The second possibility is a weak dipole allowed transition from $5s^2\,{}^1S_0$ to $5s5p\,{}^3P_1$, commonly referred to as the *red* Sr cooling transition. This transition exists because the state usually referred to as $5s5p\,{}^3P_1$ actually contains a small admixture of $5s5p\,{}^1P_1$ acquired through spin-orbit coupling. A similar process occurs in the case of ^{87}Sr, where the hyperfine coupling resulting from the nonzero nuclear spin also causes the $5s5p\,{}^3P_0$ to be coupled to both $5s5p\,{}^3P_1$ and $5s5p\,{}^1P_1$. This results in the mHz linewidth *clock* transition between $5s^2\,{}^1S_0$ and $5s5p\,{}^3P_0$. In the bosonic strontium isotopes, this transition is only open in the presence of an external magnetic field.

2.3 Blue MOT

The simplest magneto-optical trap possible with strontium is utilizing the *blue* cooling transition. Using this strong transition with a Doppler limit temperature of 730 µK, the blue MOT is the first building block of all strontium cooling schemes. Typical magnetic field gradients for this MOT range between 40 G cm^{-1} to 60 G cm^{-1} The cooling cycle between $5s^2\,{}^1S_0$ and $5s5p\,{}^1P_1$ is not completely closed as there exists a small decay channel to $5s4d\,{}^1D_2$, transferring some atoms to the $5s5p\,{}^3P_2$ and $5s5p\,{}^3P_1$ states of the $5s5p\,{}^3P_J$ triplet. Atoms that end up in ${}^3P_1$ decay back to the ground state in less than a millisecond, not leaving the capture area of the MOT in the meantime, therefore not being lost from the cooling process. However, ${}^3P_2$ is a metastable state with a lifetime of several hundred seconds [64], therefore these atoms are lost from the cooling cycle.

The ratio between the decay rate from $5s5p\,{}^1P_1$ to the ground state and that of the decay to $5s4d\,{}^1D_2$ is so high, in the order of 50000, that even in absence of any other manipulation of the atoms, the MOT will accumulate cold atoms. However, the equilibrium atom number of the blue MOT can be significantly enhanced by pumping atomic population from the ${}^3P_2$ state back to the cooling cycle. This can be achieved by employing a repumping laser at 707 nm, which excites the transition between $5s5p\,{}^3P_2$ and $5s6s\,{}^3S_1$, from where the atoms decay back to the $5s5p$ triplet. Since the $5s5p\,{}^3P_0$ state is also metastable, a second laser operating at 679 nm is needed for optimal performance. In this fashion, all atoms are pumped towards the $5s5p\,{}^3P_1$ state from which they decay very quickly back to the cooling cycle.

It is worth noting that the repumping scheme above is not the only possible one. It has been shown that the atom number of the blue MOT can be enhanced to comparable levels with several alternative repumping schemes. One of these schemes relies on repumping on the transition $5s5p\,{}^3P_2 - 5p^2\,{}^3P_2$, at 481 nm [65]. Another one uses one of the $5s5p\,{}^3P_2 - 5snd\,{}^3D_2$ transitions (n=4,5,6) with wavelengths of 3010 nm [66], 497 nm [67] or 403 nm [67] respectively, to channel the population back to the cooling cycle. Common among these methods is that the branching ratios to the $5s5p\,{}^3P_0$ state are much lower, and a suitable atom number can be reached by only using one laser for the repumping.

Typical equilibrium temperature in experimental realizations of the blue strontium MOT-s range around 1 mK to 3 mK, depending on experimental parameters. Unfortunately, these temperatures still result in a Doppler broadening of the clock transition on the 100 kHz to MHz scale, which is prohibitively large when the objective is precision spectroscopy of a transition with a linewidth in the mHz regime.

Thankfully, the atoms precooled by the blue MOT serve as an excellent starting point for a second cooling stage.

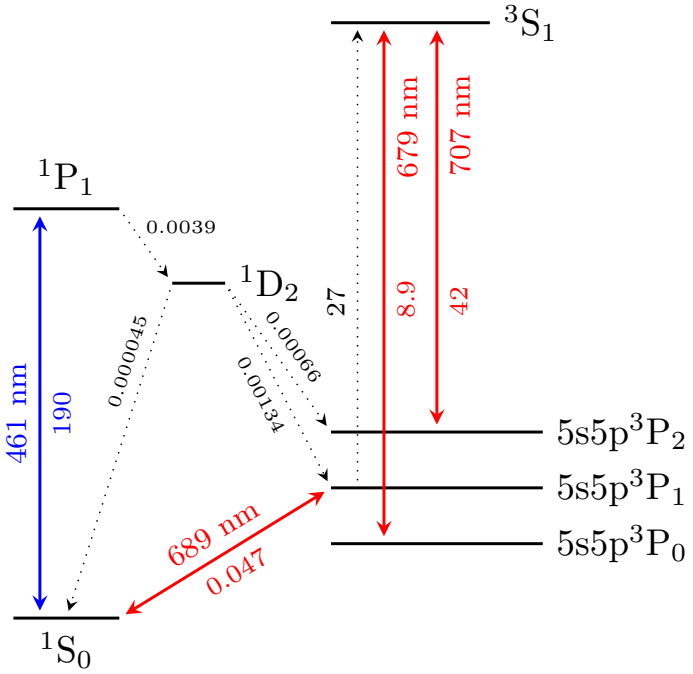

Fig. 2.2: A diagram of the energy levels and transitions relevant to the blue and red MOT-s. Decay rates are denoted in units of 2πMHz.

2.4 Red MOT

The very narrow linewidth of the red cooling transition means that, while having an extremely low Doppler limit temperature of 180 nK, it also has a very low capture velocity of 5 cm s^{-1}. This results in the issue that even the precooled atomic ensemble resulting from a blue MOT cannot be transferred directly to a red MOT, as its typical temperature corresponds to a velocity several times higher. The usual solution to this problem is to include an intermediate cooling step for efficient transfer [68], in which the linewidth of the cooling laser is artificially broadened through the use of an external acousto-, or electro-optical modulator, or direct modulation of the laser diode current, while reducing the magnetic gradient to an appropriate level typically to around 10 G cm^{-1}. After a suitable time, the broadening is ramped down to zero along with the magnetic field gradient to around 5 G cm^{-1}, and the cooling can reach its final temperature limit, which is in fact not the Doppler limit. This is because the recoil temperature of 460 nK is significantly higher than the Doppler limit, and it ends up being the limiting factor for cooling on this transition.

Samples prepared this way can then be loaded into an optical lattice, and either interrogated directly, or moved to where the interrogation will take place. As we have briefly discussed before, the two cooling cycles sharing their ground state has an important consequence for the two-stage cooling using the blue and the red transition. Since atoms in the ground state can absorb photons from the blue cooling beams, and get heated by them, they must be completely isolated from

them, to reach the much lower temperatures allowed by the red cooling cycle. This either means operating the the two cooling stages after each other, and blocking all scattered blue cooling light that could reach the atoms during the red cooling phase, or separating the two stages of the cooling spatially, and make sure to have only minimal line of sight between the two MOT-s [69].

The above described process is currently the established method of generating ultracold atomic samples for neutral atom strontium clocks. In the following we describe a different method, which relies on a second stage having the metastable state $5s5p\,^3P_2$ as a ground state instead of the atomic ground state. Most of the experimental results presented in this work is based upon this alternative method as outlined in Section 2.5.

2.5 Green MOT

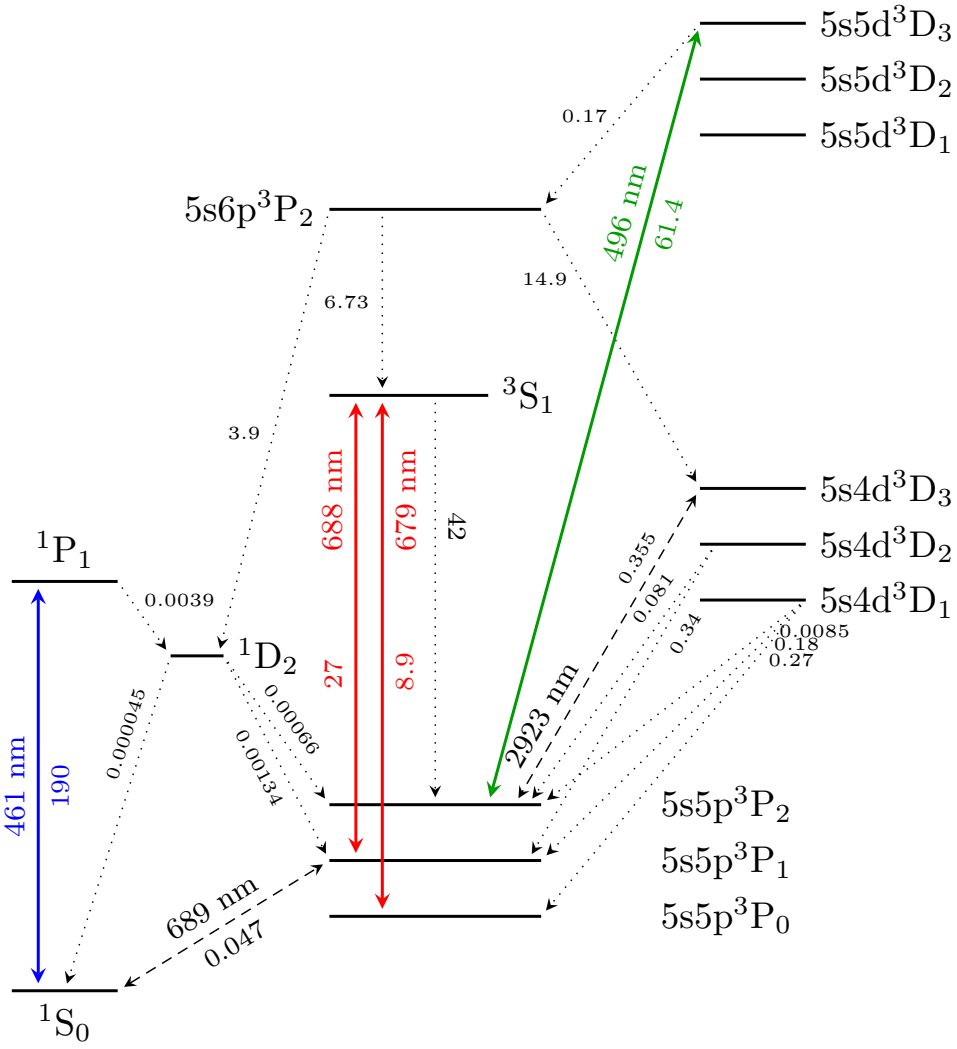

Fig. 2.3: A diagram of the energy levels and transitions relevant to the green MOT. Decay rates are denoted in units of 2πMHz.

Let us begin by identifying the relevant transitions to such an alternative MOT. We shall use the $5s5p\,^3P_2 - 5s5d\,^3D_3$ transition as our second cooling cycle , marked

green in Fig. 2.3. This alternative method has been considered several times in the literature so far [67, 70], but only a single implementation was published [71]. For some time this transition was considered unsuitable for laser cooling because of several decay channels leading to the $5s5p\,^3_1$ state where the atoms would be quickly lost from the cooling [67]. The reason for this is that the green transition, similarly to the blue one is, not completely cycling. Thus atoms are "leaking" to the $5s6p\,^3P_J$ triplet from $5s5d\,^3D_3$. The leakage rate is less favorable than that of the blue transition by a factor of about 150, and without additional measures, cooling on this transition does not accumulate cold atoms. Fortunately, by partially blocking the loss channels through the use of a repumping laser on the $5s5p\,^3P_2 - 5s6s\,^3S_1$ transition with a wavelength of 688 nm, the lifetime can be suitably extended to allow cooling and the formation of an ultracold cloud [72]. It is to be noted that, when operated in a MOT configuration, that is, three pairs of counterpropagating beams with pairwise opposite circular polarization, the green transition operates as a repumper for a blue MOT. In a single-beam configuration the repumping efficiency is too low for this transition to enhance the atom number of a blue MOT: the transition is mostly closed, meaning the atoms spend a significant time in the cycle during which time they are not restrained by any trapping force, in fact, they are being actively pushed away by the green beam. By the time they return to the ground state, they have mostly left the capture volume of the MOT, and are lost. In contrast to this, in a full MOT arrangement the atoms, while not seeing the trapping potential of the blue MOT, are in fact trapped by the green beams until they decay back to the ground state, so they can be still captured by the blue beams.

The Doppler limit temperature of 230 µK is not significantly colder as that of the blue transition, but there is a key difference in the structure of the ground states of the two cycles: the green cycle ground state has a hyperfine structure, and therefore is a candidate for sub-Doppler cooling. We will present a detailed accounting of this phenomenon in Chapter 4. Since the linewidth of the green transition is much closer to that of the blue one than the red, the simultaneous operation of both a green and a blue cooling cycle using the same magnetic gradient is possible, an important point for continuous atom generation.

2.6 Mid-infrared MOT

Analogous to the above described green transition, the $5s5p\,^3P_2 - 5s4d\,^3D_3$ mid-infrared transition at 2923 nm can also be used as a second stage cooling in a strontium MOT, but there are a few crucial differences to note in comparison. First, the transition is completely cycling, there is no additional decay channel, as there are no other lower lying energy states than $5s4d\,^3D_3$ to which the atoms could decay. Additionally, the significantly narrower linewidth results in a Doppler temperature of 1.4 µK, and since the ground state is the same, sub-Doppler cooling is also possible. Sequential cooling down to several µK-s has already been demonstrated [71, 73], including sub-Doppler cooling in one case [71].

Using this scheme is not without its drawbacks. The first issue is the wavelength of the transition itself: laser diodes with a wavelength around 3 microns are significantly more expensive and offer broader linewidths compared to the better established visible and NIR wavelength ones. The usual method is difference frequency generation, using two stabilized lasers to generate 2923 nm light. Since

the transition has a linewidth of around 47 kHz, the stabilization of two lasers to a suitable accuracy introduces significant extra complexity into the system, especially when compared to stabilizing a single laser to the MHz level as required for the green transition. Compounding the issue is the generally lower availability of optical components such as waveplates, beamsplitter cubes and dichroic mirrors in this wavelength regime. Another problem is that the narrow linewidth requires a significantly lower gradient for the working of the infrared MOT, making it nigh impossible to run in concurrently with a blue MOT in the same spatial segment using a traditional anti-Helmholtz coil configuration.

2.7 Conservative trapping potentials

The usual end goal of the MOT setups described above is to transfer the cold atoms to some conservative potential, most often a far off-resonant trap, also called a dipole trap. It is also possible to load those atoms in a low-field seeking state into a magnetic potential that has a local minimum. We shall provide a brief description of these techniques.

Magnetic trapping

Atoms with a magnetic moment can be trapped in an inhomogeneous magnetic field, by the force $\boldsymbol{F} = \boldsymbol{\nabla}(\boldsymbol{\mu} \cdot \boldsymbol{B})$ that the field exerts on the atom. The simplest form of such a trap is two coils in an anti-Helmholtz configuration. As we have mentioned in Section 2.1.2, the magnetic field of such a coil pair can be described as: $B = G\sqrt{r^2 + 4z^2}$. The potential seen by the atoms is then given by

$$U_{MT} = m_J \mu_B g_J B(x, y, z) - mgz,$$

with the coil pair axis aligned to the vertical direction (z), and the distribution of the atoms is described by the function:

$$F(x, y, z, T, \rho) = C\rho_0 \cdot exp\left(-\frac{m_J \mu_B g_J B(x, y, z) - mgz}{k_B T}\right),$$

where ρ_0 is the peak atomic density and C a norming factor. The inclusion of the gravitational potential cannot be neglected for typical quadrupole field strengths, since it will distort the trap potential as it is of comparable magnitude.

An additional issue with such a quadrupole trap is that since the magnetic field in the middle is zero, it allows for Majorana spin-flip transitions[55], which result in the atoms ending up in high-field seeking states, and being ejected from the trap. This reduces the lifetime of atoms in the trap. Should this be a problem for a given application, the zero point in the middle can be cancelled by applying a homogeneous magnetic field with a rotating direction to the quadrupole field. If the direction of this field is modulated with a frequency faster than the trap frequency, but slower then the Larmor frequency, the effect will average out and the average potential will have nonzero magnetic field strength around its minimum. This is called a *time-orbiting potential (TOP)*[74].

Optical dipole trap

Another method of trapping neutral atoms in a conservative potential is the use of high-intensity laser beams with an intensity gradient, which create the potential through the AC Stark effect: an electric dipole is induced in the atoms by the laser's electric field, which then sees a force acting on it resulting from the gradient in the electric field strength. This technique is called *far off-resonance trap (FORT)*, or *dipole trap*. The potential shift caused by the light is

$$\delta U = -\frac{E_0^2}{4}\alpha,$$

where α is the generalized dipole polarizability. α for a given state i and a given trapping laser wavelength ω_L is defined as:

$$\alpha_a = \frac{2}{\hbar}\sum_j |d_{ij}|^2 \frac{\omega_{ij}}{\omega_{ij}^2 - \omega_L^2},$$

where d_{ij} is the dipole matrix element between the states $|i\rangle$ and $|j\rangle$, ω_{ij} is the angular transition frequency between these states, and the summation goes to all $|j\rangle$ states that are dipole coupled to $|i\rangle$.

For a given transition, the differential frequency shift caused by the AC Stark shift is given by

$$\Delta\omega_{ij} = -\frac{E_0^2}{4\hbar}(\alpha_i(\omega_L) - \alpha_j(\omega_L)).$$

Should there exist a wavelength where the two polarizabilites are equal for a given transition, the differential frequency shift vanishes and the measured transition frequency will be independent of the laser intensity. This is called the *magic wavelength* for a given transition, and for the clock transition in Sr its value is at 813.4 nm.

The most basic form of a dipole trap is a laser beam focused sharply to the point where the atoms are to be accumulated. This implementation is simple to construct, but has a drawback in the fact that the trap will be much less steep along the beam as across it. If the lower trap frequency along the beam is undesired in an experiment, a crossed dipole trap can also be used, in which case a second beam or the recycled first beam is focused in the same spot.

Another way to counter this issue is to have to beams counterpropagating to each other, thereby constructing a standing wave. This is called an *(1D) optical lattice*. An optical lattice will confine the atoms along its length to the antinodes of the standing wave created by the beams. With well-chosen optical parameters, the confinement of the optical lattice is high enough that the captured atoms are in the Lamb-Dicke regime, enabling ultra-high resolution spectroscopy by suppressing the Doppler shift. As an additional advantage, slightly detuning the frequency of one of the beams, typically by using an AOM, will result in the position of the antinodes changing in time, thereby creating an *optical conveyor belt*. This can be used to transport atoms in the vacuum chamber, for example between the cooling and the spectroscopy region.

"New ideas pass through three periods:
1) It can't be done.
2) It probably can be done, but it's not worth doing.
3) I knew it was a good idea all along!"

Arthur C. Clarke

Chapter 3

A two-color continuous MOT

In the first part of this chapter we briefly describe the measurement setup, the available lasers, the vacuum chamber and other miscellaneous instruments. In the second part we present a detailed account of the measurements done on the setup, including but not limited to the results published in [75]. Theoretical calculations based on these results will be presented in Chapter 4.

3.1 Vacuum chamber

As we have detailed in Section 1.1, many of the possible future applications require the continuous atomic clock, and by extension the continuous cold atom source to be as compact as possible. Keeping this in mind, the general design of the system at the time of its creation had some differences[76, 77] compared to usual neutral atom cooling and trapping setups. The first of these is that the blue MOT is loaded directly from a Sr dispenser, there is no oven or Zeeman slower in the system, drastically reducing the power and volume requirements. The dispensers are mounted on the central copper holder depicted in Fig. 3.1 using a Macor piece. A shielding wire of 1 mm diameter is mounted in front of both dispensers to block direct line of sight of the MOT to the hot atomic beam. To our knowledge, this is the first system demonstrating direct capture of Sr atoms from a dispenser in a 3D MOT without precooling the atoms through the use of a Zeeman slower or a 2D MOT. Omitting the slower also results in a significantly lower system size, with the science chamber occupying a volume of less than 2000 cm^3.

It is also worthy of note that the system has its dual quadrupole coil pair inside the vacuum chamber. Because they are much closer to the volume where they are intended to create the proper magnetic field for the creation of the MOT, they draw significantly less current for the same gradient strength, resulting in a significantly smaller power draw and heat generation when compared to systems with external coils. Our reason for having two pairs of coils is their ability to create a structured magnetic field with a dual gradient[78] as described in Section 2.6. The coils are mounted on the central holder in a pairwise anti-Helmholtz configuration, which also allows us to remove the heat generated by them through the attached 17 mm diameter cold finger. This holder is of a hollow cylindrical construction, allowing access for the vertical cooling beams, and has 16 mm cutouts in the horizontal plane for the horizontal cooling beams. For usual currents used in our setup, air cooling the cold finger with a fan is sufficient, but water and liquid nitrogen cooling were

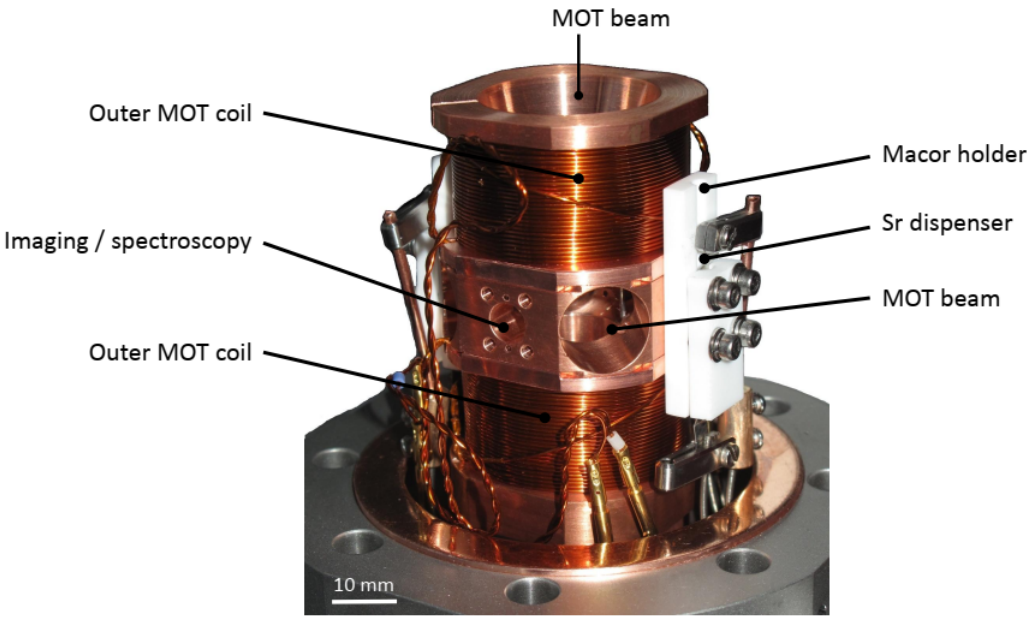

Fig. 3.1: A photo of the central copper holder.

also demonstrated.

The lower part of our vacuum system situated below the science chamber provides the mounting points for the vacuum pump (NEXTorr ion getter), the vacuum gauge (Pfeiffer IKR 270), the electric feedthrough for the coils and the dispensers, and a valve for the possible connection of a turbo pump. The bottom flange of the system and the side flanges of the science chamber are CF-40 windows, while the top window is CF-60. A cross-section of the chamber is depicted in Fig. 3.2.

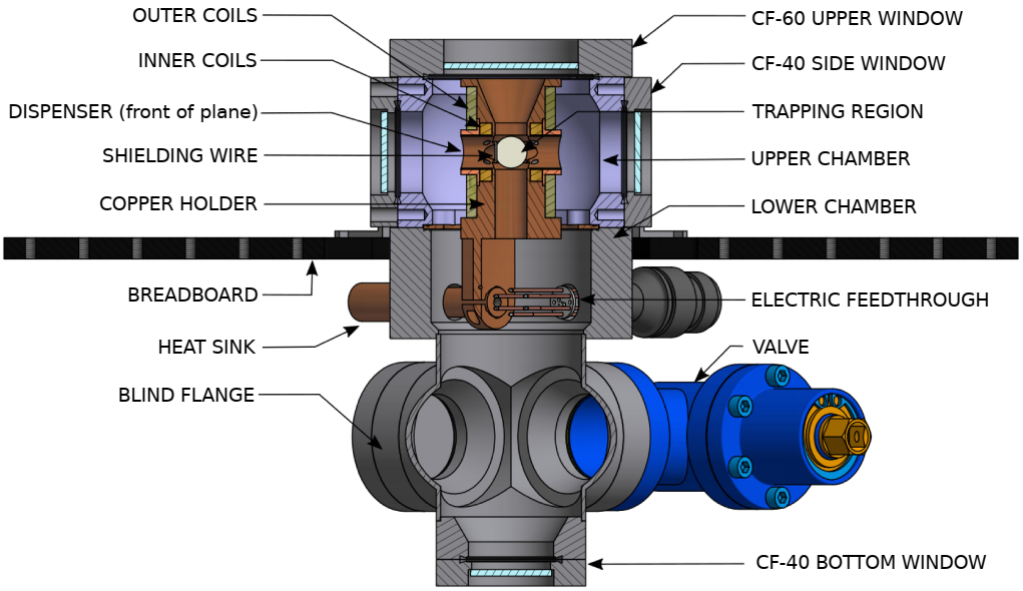

Fig. 3.2: A cross-sectional depiction of the vacuum system.

3.2 Laser and beam delivery setup

The blue (461 nm) cooling laser is frequency doubled from a 922 nm tapered amplifier (TA), using a temperature stabilized, input fiber-coupled periodically poled lithium niobate (PPLN) crystal from NTT Electronics. Between the laser and the amplifier, a small part of the beam power is split off and fiber coupled, and fed to the wavelength meter (WLM). The TA is seeded by a grating-stabilized ECDL with 12 mW of power, and is capable of emitting a maximum of 2 W of power. The blue system is capable of delivering over 40 mW of cooling light. The green (496 nm) setup is quasi-identical, with a maximum available green power being 16 mW. Additionally, it has an extra fiber coupling to a frequency comb, as the comb line intensity of the 1016 nm port is enough to provide a beat measurement at the fundamental wavelength of 992 nm when coupled with a wavemeter for the initial wavelength estimation. The optical arrangement for the two frequency doubling setups is shown in Fig. 3.3.

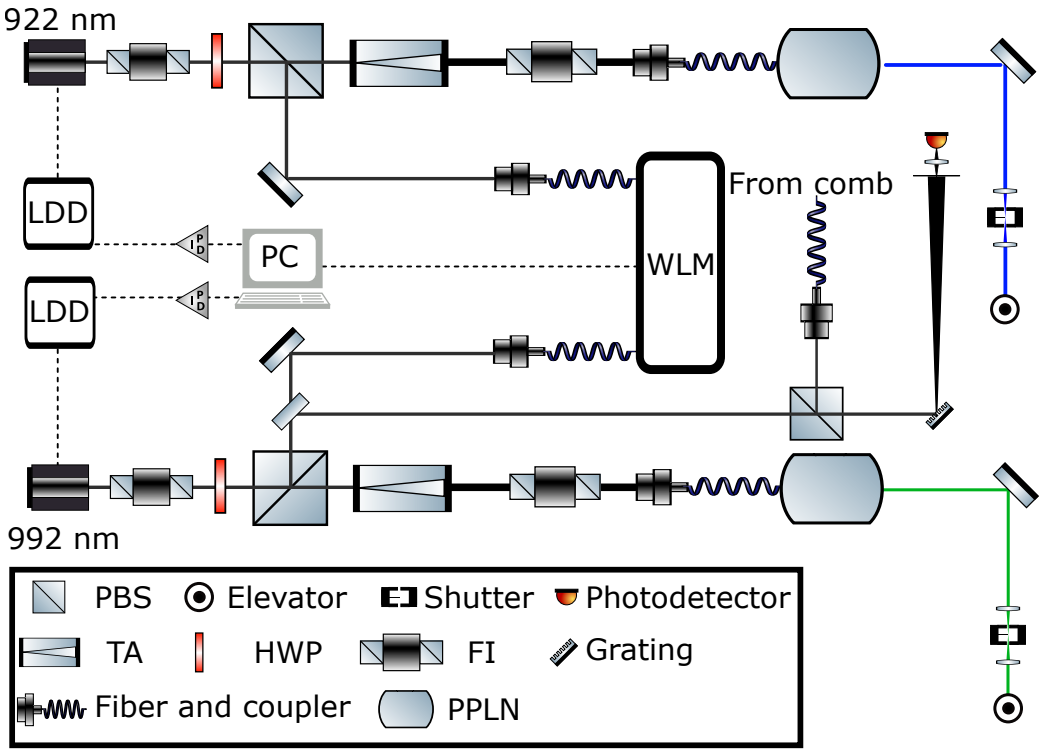

Fig. 3.3: A diagram of the frequency doubling setups. Some beam guiding mirrors were omitted for the sake of clarity.

The repumping lasers (679, 688 and 707 nm) in the beginning of our measurements were all self-built grating-stabilized ECDL-s, with the bodies of the 679 and 688 nm laser designed internally. Over the course of our measurements, the 679 nm repumper was replaced by a butterfly packaged VBG (Volume Bragg Grating) laser, which resulted in highly increased locking stability, by eliminating modehops resulting from temperature drifts. We show typical frequency stabilities for all cooling and repumper lasers in Fig. 3.4. Wavelengths and 3σ noise amplitudes are denoted in red. The blue MOT measurements shown in this work were all done with the

previous 679 nm repumper laser, while all measurements pertaining to the green MOT were made with the new one.

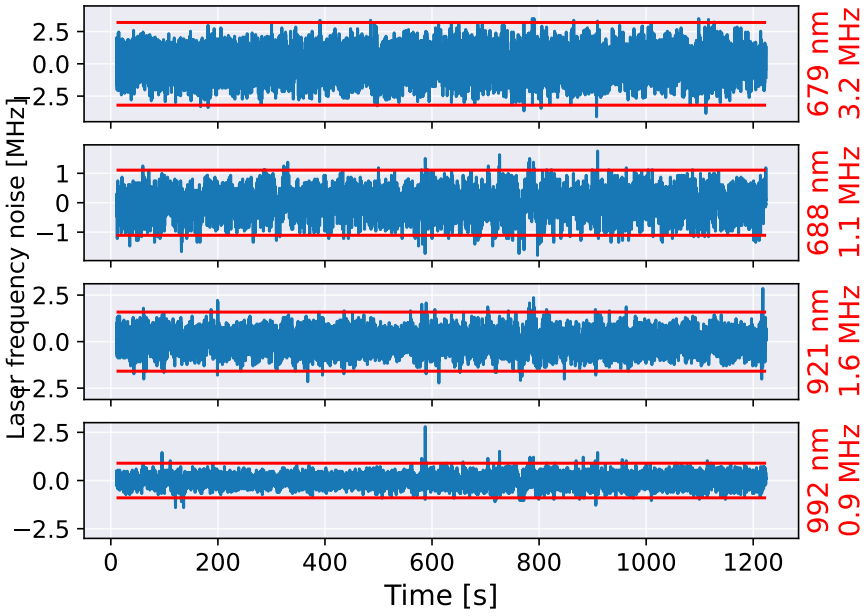

Fig. 3.4: Typical frequency stability of cooling and repumping lasers

The cooling lasers are delivered free-beam to the optical setup, whereas the repumpers are transmitted through singlemode optical fibers [76]. The reason for the free-beam delivery is that the light exiting the rectangularly cut PPLN crystal can be coupled to a singlemode fiber only with less than 30% efficiency.

All lasers are frequency stabilized using a WS8-2 wavelength meter from the company HighFinesse. The device is equipped with an endlessly singlemode 8-channel switch and a PID module built into the PC controlling the WS8-2. This allows the quasi-simultaneous frequency stabilization and monitoring of up to seven lasers, while the eighth port is reserved for the calibration laser. The wavemeter has a specified absolute accuracy of 10 or 30 MHz depending on the wavelength, and a relative accuracy of 200 kHz. Since the optimal absolute values of the frequencies can be determined based on the MOT parameters, the absolute error of the device is irrelevant for our purposes, provided said error stays constant over time. In our observation this was true for the years that we have performed our measurements, which is consistent with literature experience of the device [79, 80], which show less than 2 MHz deviation over time from the original absolute error. The locking bandwidth of the wavemeter (down to a few Hz with multiple lasers controlled) is only suitable for long-term locking, the linewidths of the lasers are practically unaffected by the wavemeter lock. Since all the lasers have a linewidth at least a factor of 5 below the respective (in some cases broadened) transition linewidths, this does not cause any problems.

We perform the frequency calibration of the WLM to an SL03 stabilized helium-neon laser from SioS Meßtechnik. The laser is certified for 5 MHz absolute accuracy, which in our experience was suitable for the wavemeter to reach the required frequency stability in day-to-day operation. This is explained by the fact that the initial offset in the absolute accuracy is negated through the process of determining the optimal frequencies locally, and only the stability of the laser is relevant.

Both cooling beams are turned on and off with a mechanical shutter in the center of a 1:1 telescope, using identical Thorlabs LBF254-040-A *best form lenses* with a focal length of 40 mm. These lenses have two curved surfaces of different curvature radii, in a way that spherical aberration and the size of the focal spot for a given focal length is minimized. According to the manufacturer's specifications, they are suitable for near-diffraction limited performance with a Gaussian input beam. With the shutter blade intersecting the beam in the focus and in the middle of its own motion range where its moving with the highest speed, it sweeps the full beam in under 30 µs. We've found this to be sufficiently quick not to affect the MOT negatively.

Beam diameters are 12 and 4.5 mm for blue and green respectively. These are set using a Galilean telescope for each of the beams. The lenses of the telescopes are slightly offset from the standard confocal position to compensate for the slight divergence of the beam resulting from the small emission aperture of the PPLN crystals. We divide the green and blue trapping beams into three beams of approximately equal intensity using two half-wave plates (HWP) and two polarizing beamsplitter cubes (PBS), then we set the polarization of each beam to circular using a quarter wave plate (QWP). Each blue beam is overlapped with a green one using a dichroic mirror (DM), sent into the vacuum cavity in orthogonal directions, and then retroreflected with an achromatic quarter wave plate (QWP).

We have chosen a wavelength of 1064 nm (the deviation from the usual magic wavelength of 813 nm is explained later) for our dipole trap, and use a 50W laser from Azurlight Systems (ALS 1064 50 I SF). The beam shaping setup is shown in Fig. 3.5. The beam emitted by the laser head is sent through an AOM (TF950-500-

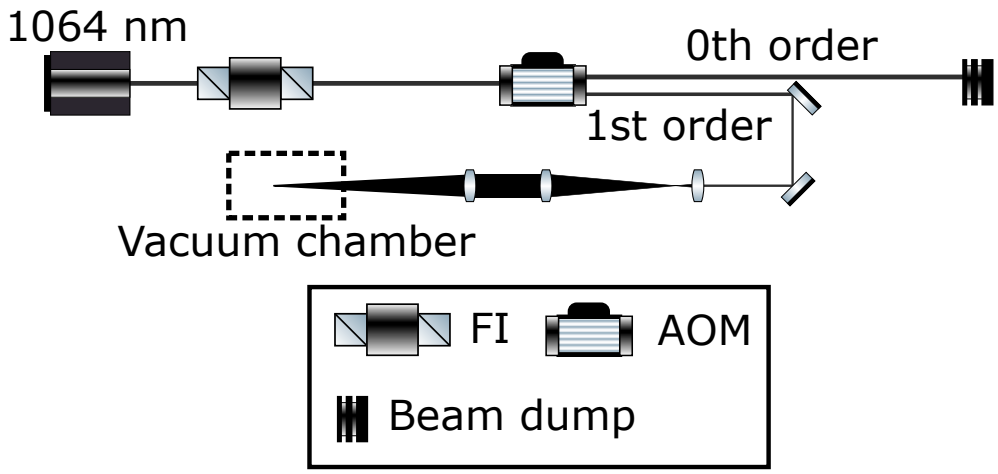

Fig. 3.5: The dipole trap laser setup

1-5-NT2) for mode cleaning and to allow us to trigger it with high speed. After this, it is focused on the MOT with a lens assembly consisting of Thorlabs achromatic doublets (AC-254-050-B-ML, AC-254-500-B-ML, AC-254-300-B-ML). The focusing assembly achieves a minimum Gaussian beam waist of 17 µm.

The maximum achievable power reaching the atoms is over 6W, which is limited by thermal lensing effects in the AOM. As we will see later, this is sufficient for capturing a significant amount of atoms from the MOT.

We monitor our atomic clouds using fluorescence and absorption imaging. Fluorescence images are acquired using a DCC1240M Thorlabs camera, and a Computar

MLH-10X manual zoom objective mounted at an oblique angle to the chamber. Fluorescence imaging was used for general rough adjustment of the MOT, for preliminary determination of the optimal frequency and intensity working point of each laser and for monitoring of the adjustment drift while measuring.

For absorption imaging we use light split off from the main green cooling beam, that is sent through two AOM-s to shift the frequency back to resonance, while also providing a convenient method for toggling the imaging beam. This is then fiber coupled, and transferred to the MOT, where a beam of 10 mm diameter is created with a fiber collimator. This beam is aimed at the MOT at a five degree angle along one of the cooling beams. After passing through the vacuum chamber it is collected by an achromatic doublet of 75 mm focal length and sent to the absorption imaging camera, a Thorlabs DC3240M. This way the setup achieves a 2f-2f absorption imaging of the magneto-optical trap, which we used to measure the 2D density distribution of the MOT, and to determine the temperature through ballistic expansion time-of-flight series. The final optical adjustment of the MOT was also performed using the absorption imaging.

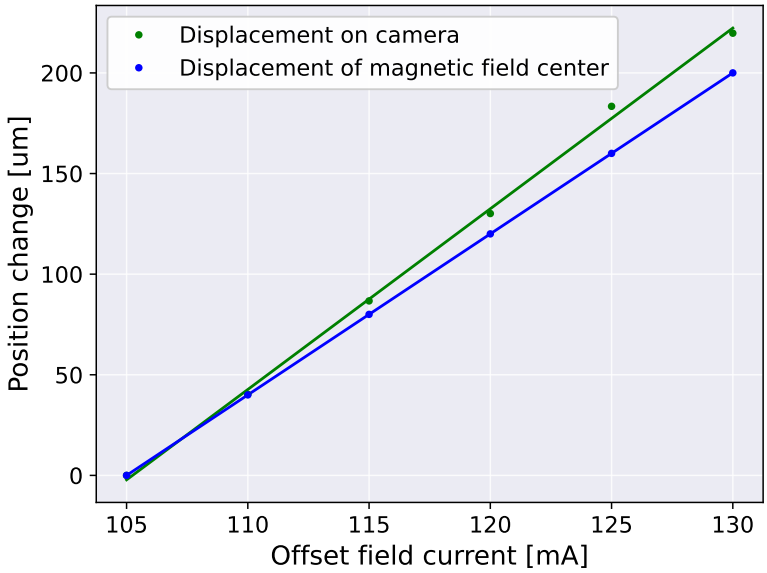

Fig. 3.6: Magnification factor determination.

The usual way of calibrating the imaging magnification by letting the cloud freefall and calculating it from the movement of the center of mass is infeasible in our case, since the low atom numbers mean the cloud center of mass can be only determined with a reasonable accuracy up to only about 2 ms of free fall. In this time the freefall would move the cloud about 20 micrometers, which is less than four pixels on the camera. Instead, we have employed the following calibration method:

- Since the quadrupole field coils were calibrated before being built into the chamber, we can calculate the magnetic field based on the currents introduced to them.
- The atomic cloud in the magnetic trap will have its center at this point.
- By switching the outer coil pair to Helmholtz configuration we can apply an offset field and move the trap center.

- Comparing the change of position on the camera with the calculated absolute position change gives us the magnification.
- The effect of the earth magnetic field is only a constant offset in the position of the magnetic field, which we can safely ignore since we only calculate relative positions.

The results of this process are shown in Fig. 3.6. The magnification is established by this method as 1.12. Additionally, because of the low atom number, we apply the image processing algorithm described in [81]. An overview of the optical setup is show in Fig. 3.7.

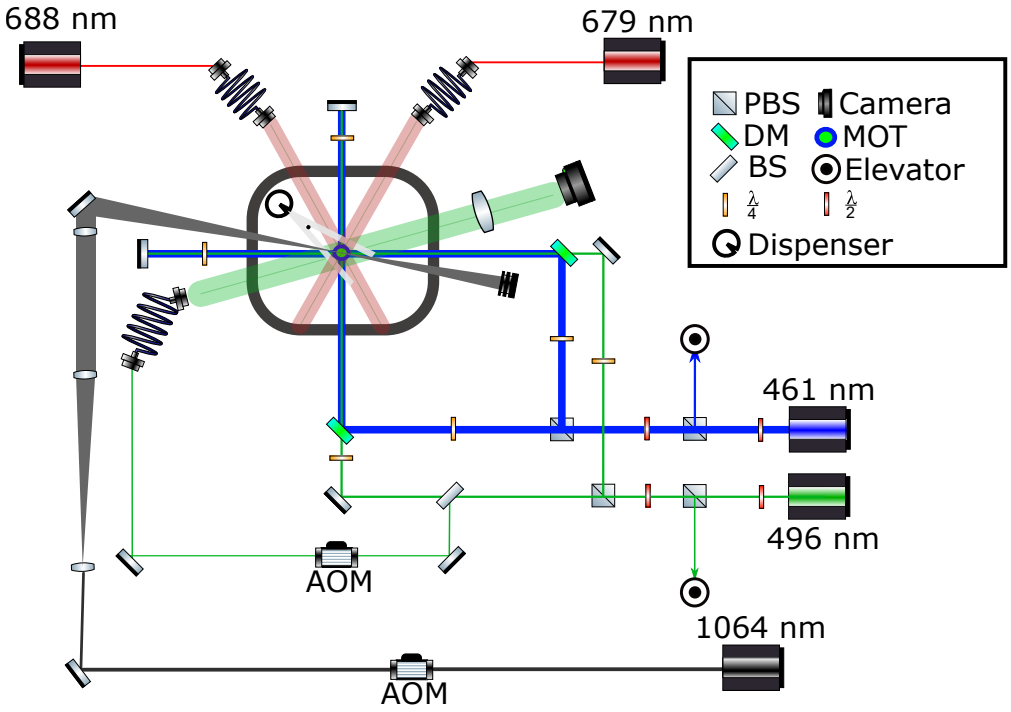

Fig. 3.7: A diagram of the optical arrangement. Some beam guiding mirrors were omitted for the sake of clarity.

3.3 Timing

Ballistic expansion temperature measurements require precise timing control on the 10 µs level. This task cannot be accomplished by leaving the timing to the computer, therefore specialist equipment needs to be used. In our system, all precision timing tasks are controlled by an ADwin Pro II using a T11 processor module, allowing us to control 32 digital output channels with a resolution of 4 µs. These channels control the cooling beams through the trigger inputs of the shutter controller, the quadrupole coils through the trigger input of the coil current drivers, the imaging AOM-s and the AOM of the dipole trap laser. The controller is also equipped with analog voltage outputs, which we use to control the current of the coils through the modulation input of their driver. The system also interfaces with the wavemeter running on a Windows computer using a TCP/IP interface to enable control of the wavelengths the lasers are being locked to. The ADwin device itself is programmed by a PC, using the *qcontrol3* measurement control system which was created in the Max Planck Institute of Quantum Optics by Christoph Gohle, Christian Gross and Sebastian Blatt. The timing diagrams for all measurements are shown in Fig. 3.8.

A typical ballistic expansion measurement as implemented in our lab contains the following steps, all fully automated:

1. Check that the calibration of the wavemeter is correct, if not, recalibrate
2. Initiate the frequency lock of all lasers, check if all of them locked successfully, if not, warn the user
3. Measure half of the assigned time-of-flight series
4. Tune the blue cooling laser away from the cooling wavelength to extinguish the MOT
5. Record a background measurement that we use to subtract persistent features from the measurement
6. If the magnetic trap is being measured as well, execute that measurement
7. Measure the remaining half of the time-of-flight series

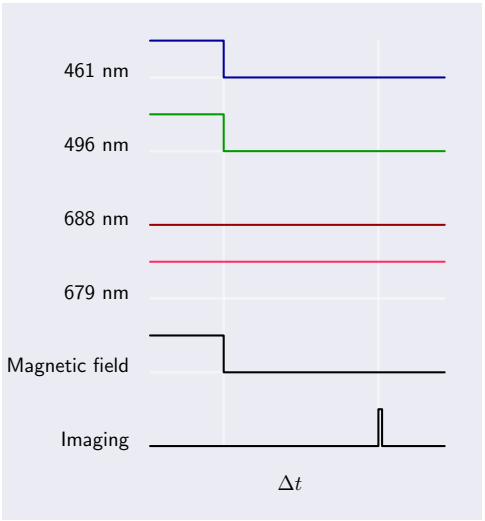

(a) Blue

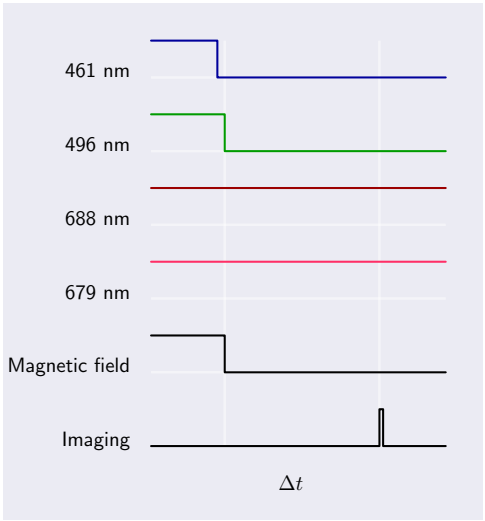

(b) Green

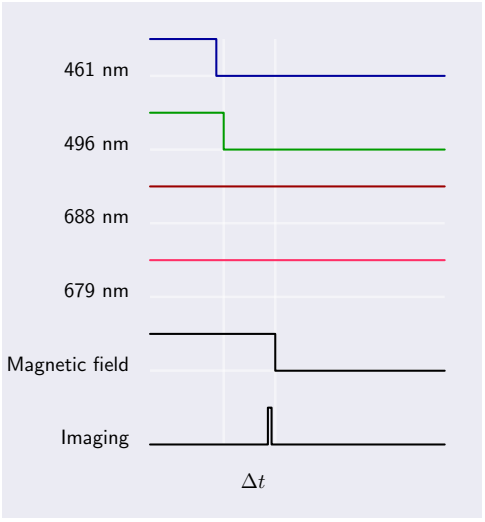

(c) Magnetic trap

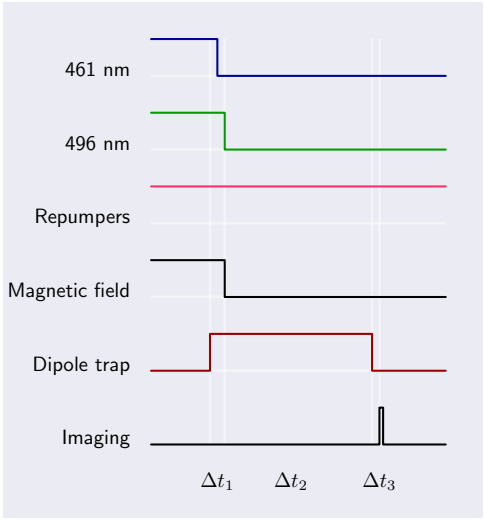

(d) Optical dipole trap

Fig. 3.8: Timing diagrams of our measurements

3.4 Preliminary measurements

3.4.1 Blue MOT

For the realization of a blue MOT, our current system uses the $5s5p\,^3P_2 - 5s5d\,^3D_3$ transition at 496 nm to repump instead of the usual $5s5p\,^3P_2 - 5s6s\,^3S_1$ at 707 nm. The technique relies on the fact that, with the $5s5p\,^3P_1$ not being actively pumped out, atoms that reach this state will quickly decay back into the ground state. This decay channel was the original reason why the creation of a green MOT was considered impossible [67].

As mentioned in Section 2.1.2, repumping on this transition only works if the beams are arranged in a MOT configuration, both spatially and with regard to the polarization. If not spatially confined, most of the atoms leave the capture volume by the time they are cycled back to the ground state. This technique was first documented by Katori [21] to facilitate atom transfer between the blue and the red MOT in their setup.

For absorption imaging measurements of the blue MOT, we used a second 461 nm laser tuned to resonance directly with the wavemeter. All other components were set up the same as way described in Section 3.2.

For optimal atom transfer into the green MOT, we have measured the temperature and atom number characteristics of the blue cloud depending on cooling laser intensity and detuning.

Temperatures of the blue MOT were calculated using the standard ballistic expansion time-of-flight measurement technique as detailed in Section 2.3.

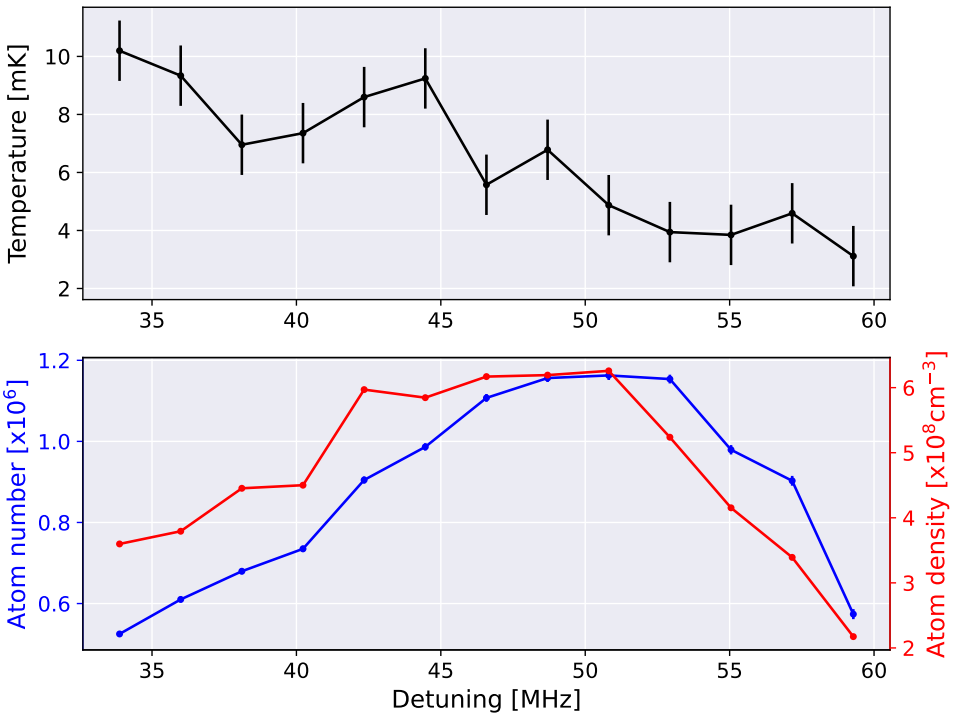

Fig. 3.9: The temperature, atom number and atom density of the blue MOT as a function of the cooling laser detuning.
$I = 7\ \mathrm{mW/cm^2}, G = 57\ \mathrm{G/cm}$

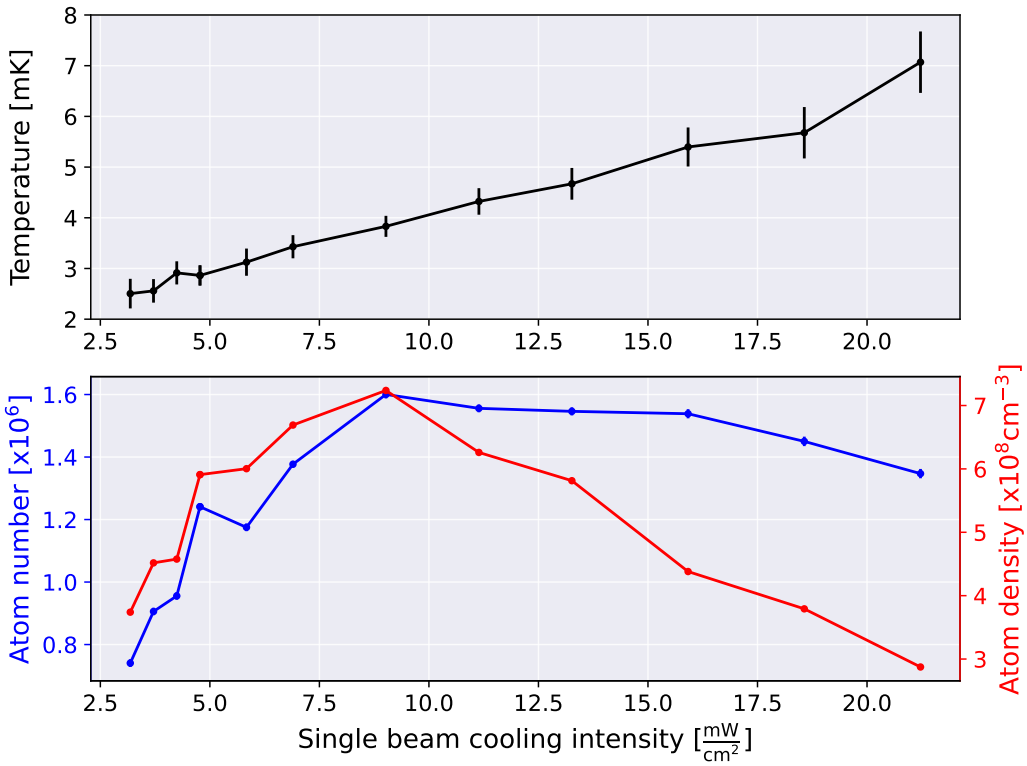

Fig. 3.10: The temperature, atom number and atom density of the blue MOT as a function of the single beam cooling laser intensity.
$\delta = 51\text{MHz}, \text{G} = 57$ G/cm

In the end, we have selected the following standard parameters for the operation of the blue MOT:

- Single beam cooling intensity: $\text{I} = 9$ mW/cm^2
- Cooling laser detuning: 51 MHz ($\approx 1.6\gamma$)
- Magnetic field gradient: 57 G/cm

These parameters were used for all measurements regarding the green MOT.

We have also modeled the population kinetics of the MOT with a 496/679 nm repumper configuration, based on the following differential equation system containing the relevant states. The Sr states relevant to us are numbered as follows:

0	$5s^2\ ^1S_0$
1	$5s5p\ ^1P_1$
2	$5s4d\ ^1D_2$
3	$5s6s\ ^3S_1$
4	$5s5p\ ^3P_2$
5	$5s5p\ ^3P_1$
6	$5s5p\ ^3P_0$
7	$5s6p\ ^3P_2$
8	$5s4d\ ^3D_3$
9	$5s4d\ ^3D_2$
10	$5s4d\ ^3D_1$
11	$5s5d\ ^3D_3$

With that numbering, the differential equation system to be solved is as follows:

$$
\begin{aligned}
\dot{N}_0 &= \Phi_B + \gamma_{1\to0}N_1 + \gamma_{2\to0}N_2 + \gamma_{4\to0}N_4 + R_{461}(N_0 - N_1) + \beta_B N_0^2 \\
\dot{N}_1 &= R_{461}(N_0 - N_1) - (\gamma_{1\to0} + \gamma_{1\to2})N_1 \\
\dot{N}_2 &= \gamma_{1\to2}N_1 + \gamma_{7\to2}N_7 - (\gamma_{2\to0} + \gamma_{2\to4} + \gamma_{2\to5})N_2 \\
\dot{N}_3 &= \gamma_{7\to3}N_7 + R_{688}(N_5 - N_3) + R_{679}(N_6 - N_3) - (\gamma_{3\to4} + \gamma_{3\to5} + \gamma_{3\to6})N_3 \\
\dot{N}_4 &= \gamma_{2\to4}N_2 + \gamma_{3\to4}N_3 + \gamma_{11\to4}N_{11} + \gamma_{8\to4}N_8 + \gamma_{9\to4}N_9 + \gamma_{10\to4}N_{10} - R_{496}(N_4 - N_{11}) - \beta_G N \\
\dot{N}_5 &= \gamma_{2\to5}N_2 + \gamma_{3\to5}N_3 + \gamma_{8\to5}N_8 + \gamma_{9\to5}N_9 - R_{688}(N_5 - N_3) - \gamma_{5\to0}N_5 \\
\dot{N}_6 &= \gamma_{3\to6}N_3 + \gamma_{10\to6}N_6 - R_{679}(N_6 - N_3) \\
\dot{N}_7 &= \gamma_{11\to7}N_{11} - (\gamma_{7\to2} + \gamma_{7\to3} + \gamma_{7\to8} + \gamma_{7\to9} + \gamma_{7\to10})N_7 \\
\dot{N}_8 &= \gamma_{7\to8}N_7 - \gamma_{8\to4}N_8 \\
\dot{N}_9 &= \gamma_{7\to9}N_7 - (\gamma_{9\to4} + \gamma_{9\to5})N_9 \\
\dot{N}_{10} &= \gamma_{7\to10}N_7 - (\gamma_{10\to4} + \gamma_{10\to5} + \gamma_{10\to6})N_{10} \\
\dot{N}_{11} &= R_{496}(N_4 - N_{11}) - (\gamma_{11\to4}\gamma_{11\to7})N_{11}
\end{aligned}
$$

Where $\gamma_{i\to j}$ is the decay rate from state i to state j, N_i is the population of state i, β_B and β_G are the two-body loss rates for atoms in the $5s^2\,{}^1S_0$ and $5s5p\,{}^3P_2$ states respectively and Φ_B is the atom flux captured from the thermal beam into the blue MOT.

We solved the system numerically, and fit the free parameters ϕ_B and β_B on the measured loading curve of the blue MOT as shown in Fig. 3.11:

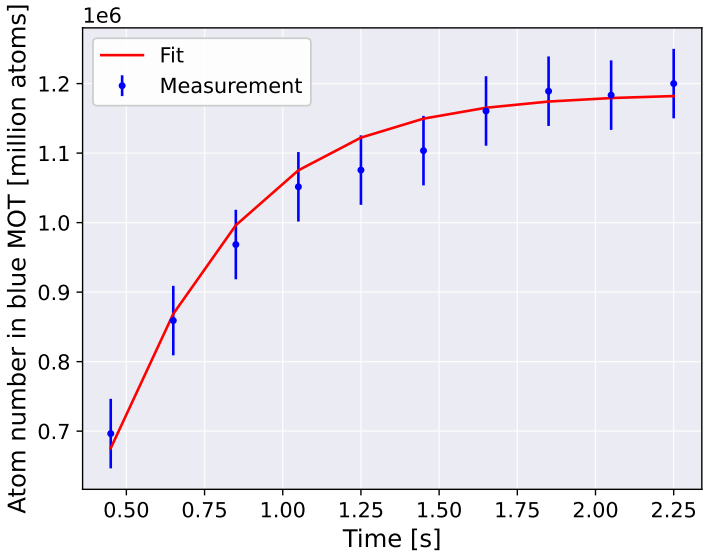

Fig. 3.11: A loading curve of the blue MOT taken with the standard parameters,

We find the captured atomic flux from the MOT to be $\Phi_B = 3.0 \cdot 10^6 \pm 2.2 \cdot 10^4$ atoms, while the two-body loss rate is $\beta_B = 1.65 \cdot 10^{-6} \pm 2.3 \cdot 3^{-8}$.

3.5 Green MOT

By using the 688 nm laser to pump the $5s5p^3P_1$ state to the $5s6s^3S_1$ and thereby maximizing the population of the $5s5p^3P_2$ state, we can increase the average time

the atoms spend in the green cooling cycle, which results in the formation of a green cloud. It is an important result already foreshadowed in [76] that the green MOT can be created in a magnetic field gradient suited for the blue MOT. We have studied this MOT extensively, and will now present our major findings.

3.5.1 Non-Gaussian temperature distribution

As described in Section 2.5, the fact that sub-Doppler cooling will not work on the whole of the green MOT, only on certain velocity classes will result in the atoms developing a velocity distribution that is distinctly non-Gaussian. This phenomenon is documented in the literature for several atomic species [82, 83, 84, 85].

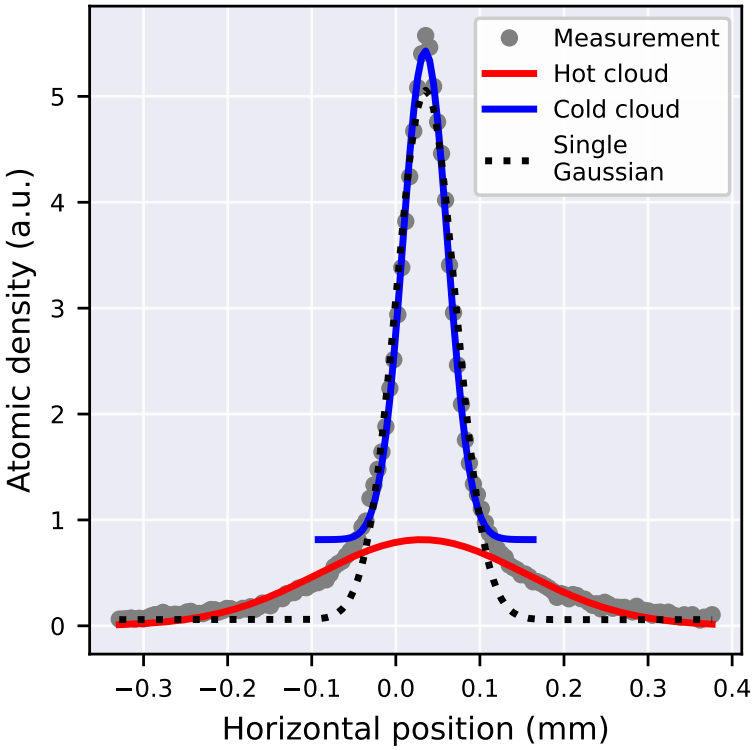

Fig. 3.12: Horizontal density distribution of the green atom cloud.
s=0.35, $\delta = 19$ MHz G $= 57$ G/cm
The distribution is fitted with both a single Gaussian and the sum of two

As it can be seen in Fig. 3.12, the atoms separate into two distinct clouds overlapping each other, suggesting also two distinct components of the velocity distribution. For an atomic cloud with this type of distribution, the standard protocol of ballistic expansion as described in Section 2.5 needs to be changed, as the fitting of a single Gaussian would clearly not sufficiently capture the characteristics of the cloud. For this reason, we evaluated the green MOT measurements by fitting the sum of two Gaussians on the density distribution, and we designate them the "cold" and the "hot" cloud from now on. Temperatures are calculated for the hot and cold cloud separately, their velocity distributions denoted by $F_c(v)$ and $F_h(v)$. We are also introducing a metric called "equivalent temperature" for the MOT: after getting the temperatures of the two clouds, we construct the velocity distribution $F(v)$ of

the whole MOT by summing up $F_c(v)$ and $F_h(v)$ weighted by the measured atom number of the two clouds. After this, the expected value of the squared velocity $\langle v^2 \rangle$ can be calculated from $F(v)$. Finally the equivalent temperature is calculated in the following way:

$$T_{eq} = \frac{m_{Sr} \langle v^2 \rangle}{k_B}.$$

We summarize the results of the MOT temperature dependence of cooling laser intensity and detuning in Fig. 3.13 and Fig. 3.14.

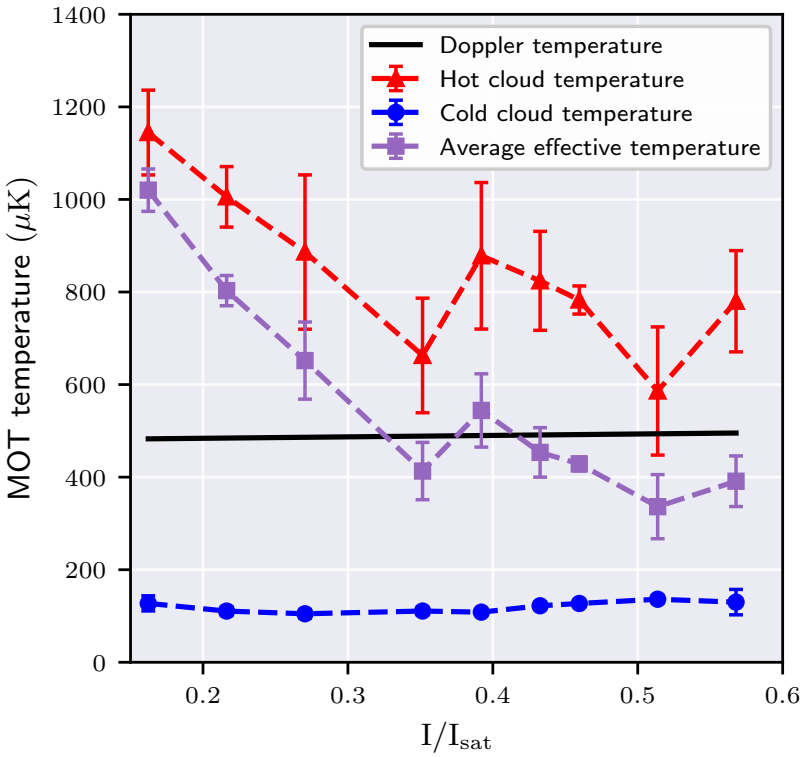

Fig. 3.13: The temperature of the green MOT as a function of the saturation parameter.
$\delta = 19$ MHz, G = 57 G/cm

It can be seen that the warm cloud shows the expected behaviour of Doppler cooling, approaching the Doppler limit with increasing intensity. The temperature of the colder cloud, in contrast, varies much less with intensity and has a minimum at $I/I_{sat} = 0.39$. The existence of this minimum temperature is consistent with the theory of sub-Doppler cooling (see Chapter 4).

Similarly, the dual fit also allows us to take a look at the atom numbers in the two clouds, pictured in Fig. 3.15.

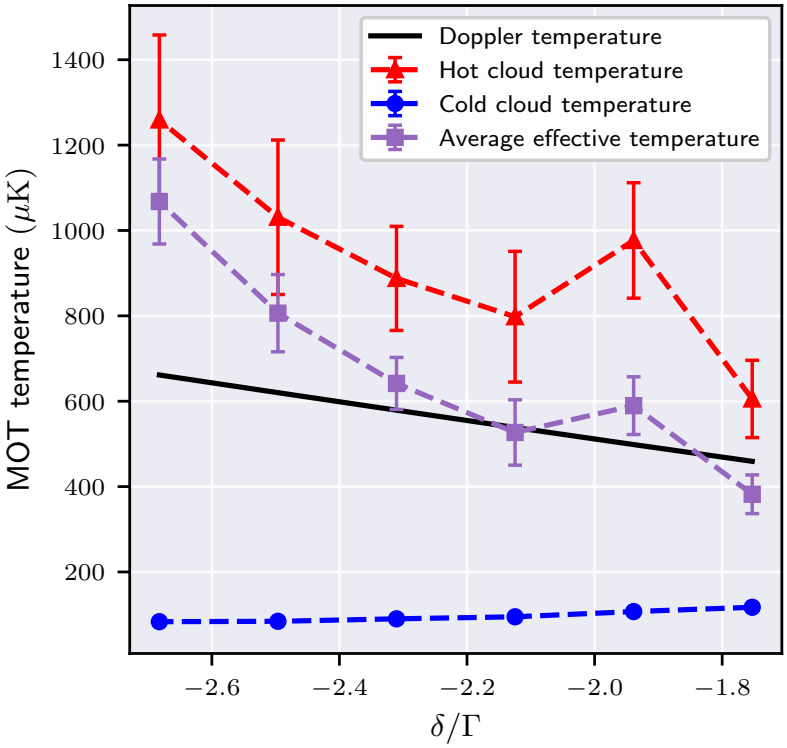

Fig. 3.14: The temperature of the green MOT as a function of the frequency detuning.
$I/I_{sat} = 0.4$ G = 57 G/cm

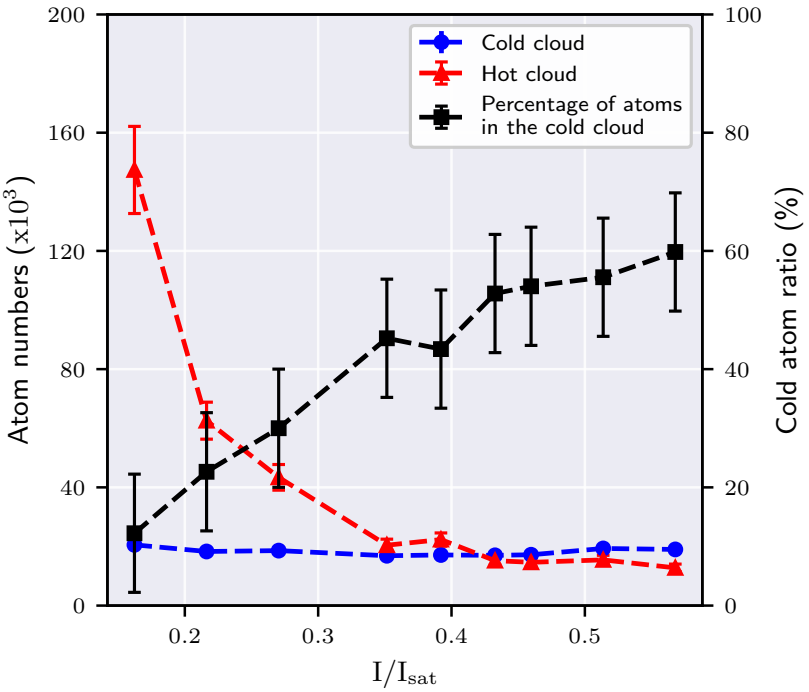

(a) Intensity

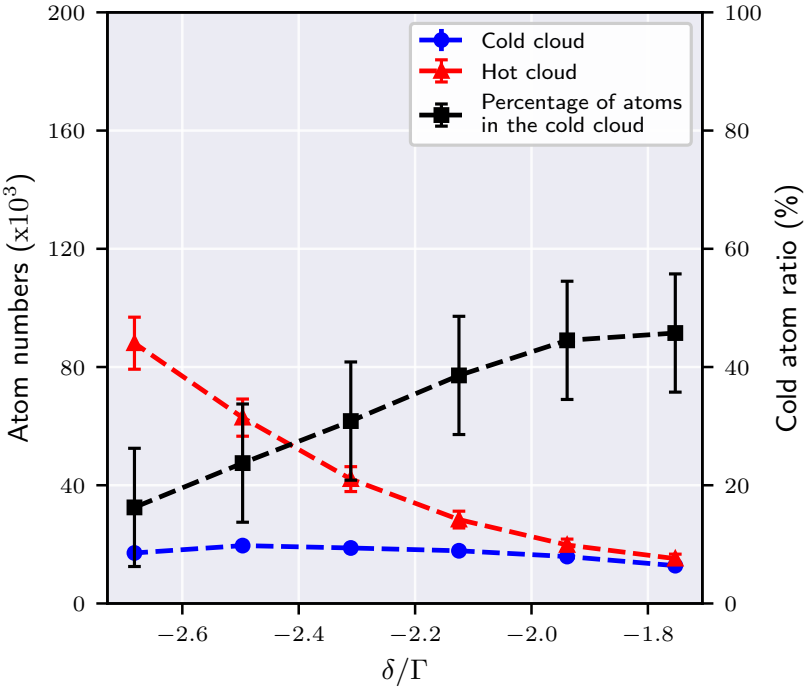

(b) Detuning

Fig. 3.15: The atom numbers of the two clouds as a function of single beam cooling intensity and cooling laser frequency detuning

An interesting result is that the population of the hot atom cloud is reduced significantly both with increasing cooling intensity and decreasing detuning, while that of the cold cloud stays approximately constant. This, coupled with the fact that with a higher cooling intensity or smaller detuning more velocity classes of the warm cloud are transferred to the sub-Doppler cooling process, suggests that the atom number of the cold cloud is limited by its higher density, and the resulting losses.

Calculated atomic densities for the cold cloud are typically $\rho \approx 2 \cdot 10^{10}$, a factor of 30 higher than those for the blue MOT. The typical densities of the hot cloud in comparison are of the same order of magnitude or lower than the blue MOT, especially at higher intensities when the atom number of the hot cloud drops sharply.

In addition to the previous measurements, we have also measured the lifetime of the green MOT depending on the cooling laser intensity. It is the easiest way to determine the expected atomic flux that can be transferred to the moving lattice for the continuous extraction later. In steady state, the influx of atoms from the blue MOT and the green MOT losses are in dynamic equilibrium:

$$\frac{dN}{dt} = \Phi_{BMOT} - N/\tau = 0,$$

which means the incoming atom flux from the blue MOT equals the loss rate from the green MOT. Assuming a suitable extraction technique with extraction efficiency η_{ex}, the amount of atom flux the green MOT can load into an optical lattice is $\eta\Phi_{BMOT}$. We find that $\Phi_{BMOT} = 1.6 \cdot 10^6 \pm 10^5$ atoms per second, independent of the green cooling laser intensity, which means over half of the atoms captured by the blue MOT are transferred to the green MOT in continuous operation. Clock spectroscopy techniques typically do not require a large amount of atoms in the optical lattice, since on average less then an atom per lattice antinode is desired, the calculated flux leaves allowance for a significant technological factor in η_{ex}.

We have also measured the lifetime of the green MOT depending on the intensity of the 688 nm repumper laser. As it can be seen in Fig. 3.16b, the lifetime of the MOT does significantly depend on this intensity. Indeed, as we have mentioned in the beginning, without a 688 nm laser the atoms do not spend enough time in the MOT to coalesce into a cloud. However, we can also see that further increasing the intensity would offer no further gains on this front, as the cloud lifetime does saturate, contrary to the assertion in [71].

Access to an absolute reference in the form of a Toptica zero offset frequency comb consisting of a DFC CORE+ unit with 80 MHz repetition rate and a DFC SCIR extension module with a center wavelength of 1020 nm, referenced to a GPS disciplined rubidium frequency standard (GPS10RBN from Precision Test Systems) allowed us to determine the absolute frequency of the $5s5p\,^3P_2 - 5s5d\,^3D_3$ transition. The spectroscopy was performed by tuning the AOM shifts between the cooling and the imaging beam to change the imaging beam frequency around the resonance. The cooling lasers and the magnetic coils were turned of 1 ms before the imaging so that Zeeman and light shifts caused by them could be eliminated.

The absolute frequency of the green cooling laser was determined by a beat measurement of its fundamental frequency to the frequency comb which has a specified fractional instability of 10^{-11}, which in our case translates to an absolute error of $\sim$ 3 kHz. The AOM-s used to shift the green frequency back towards resonance

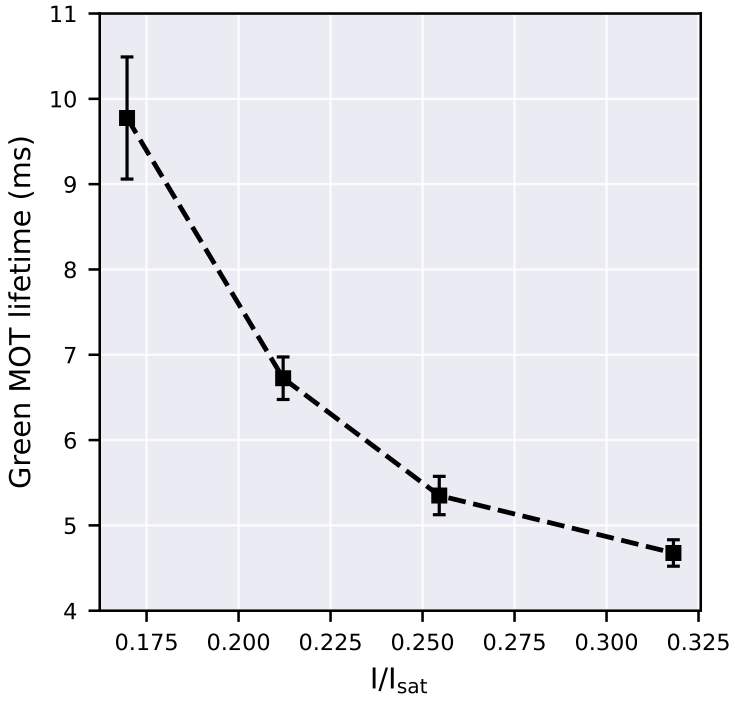

(a) Green cooling laser

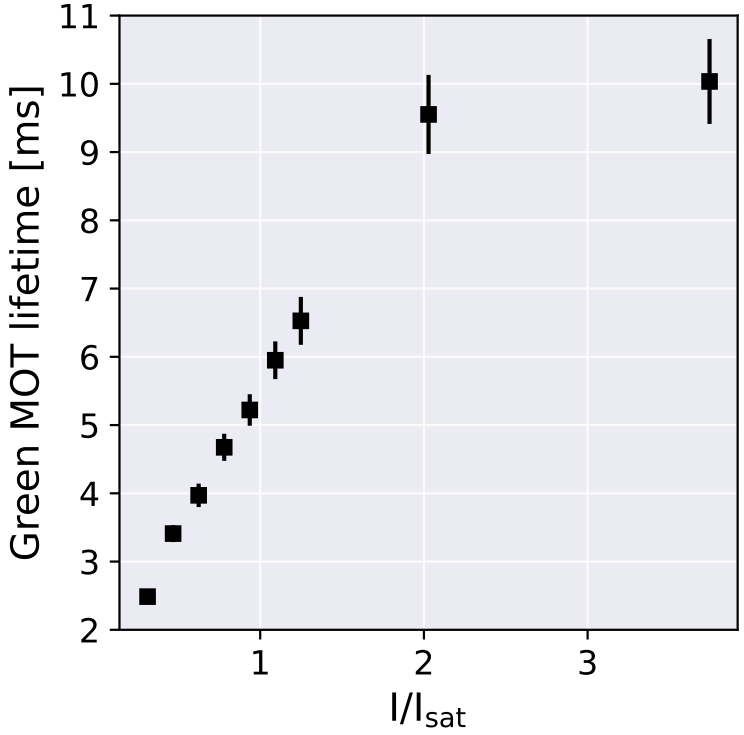

(b) 688 nm repumper

Fig. 3.16: Green MOT lifetimes as a function of various laser intensities.

are controlled by a Rigol DG4102 waveform generator, while the beat frequency measurement is done with a Signal Hound BB60C spectrum analyzer. Considering the error of the Lorentzian fit, the various instrument errors and the Zeeman shift

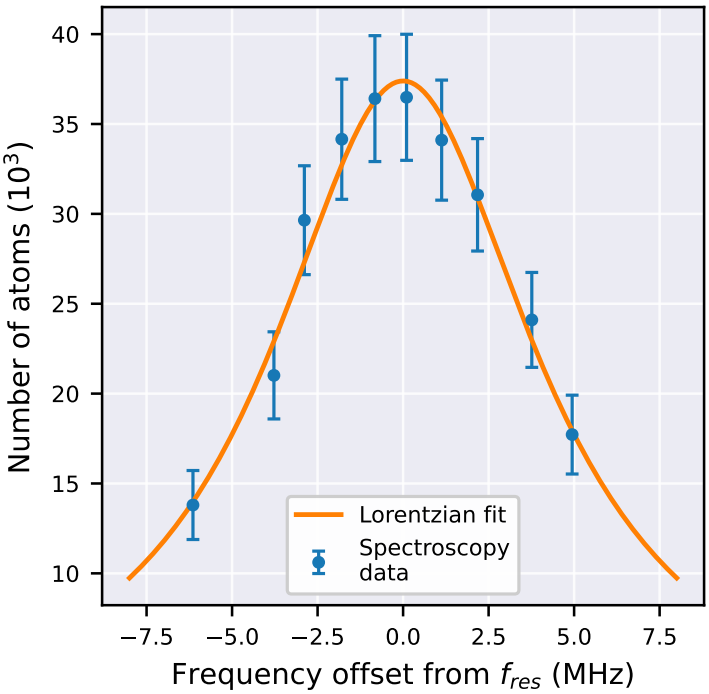

Fig. 3.17: Absorption spectroscopy of the green transition in the dipole trap

resulting from the Earth's magnetic field, we estimate the total absolute error to be less than 2 MHz. Altogether we have measured the absolute frequency of the green transition to be 603 976 473 MHz with a total absolute accuracy error below 2 MHz.

3.6 Magnetic trap

Using the $5s5p^3P_2$ state as the ground state for our second cooling cycle does offer another interesting possibility. Magnetic trapping of bosonic strontium is not possible using the base state, since it has zero magnetic momentum. It is well known from earlier research [86, 87] that during the operation of a standard blue MOT, if not pumped out, the atoms in the $^3P_2$ state will be gathered in a linear magnetic trap created by the quadrupole field of the MOT. Unfortunately, without further cooling these atoms are too hot to be loaded into a lattice without using prohibitively high laser intensities. However, turning the blue and green cooling lights off but leaving the quadrupole field on in our system does present us with the opportunity the create a cold sample of bosonic strontium trapped in a magnetic trap.

The timing diagram of the magnetic trap measurements is shown in Fig. 3.8c.

Having a calibration of the magnetic field of the coils allows us to calculate the density distribution in the trap potential with only the temperature and the atom number as fitting parameters. Our fitting function is:

$$F(x,z,T,N) = \frac{N}{c} \cdot exp\left(\frac{m_J \mu_B g_J B(x,z) - mgz}{k_B T}\right), \tag{3.1}$$

Where $g_J = 3/2$ for the $5s5p^3P_2$ state, c is a factor related to the optical absorption cross-section and camera pixel size. The magnetic trap is populated only from

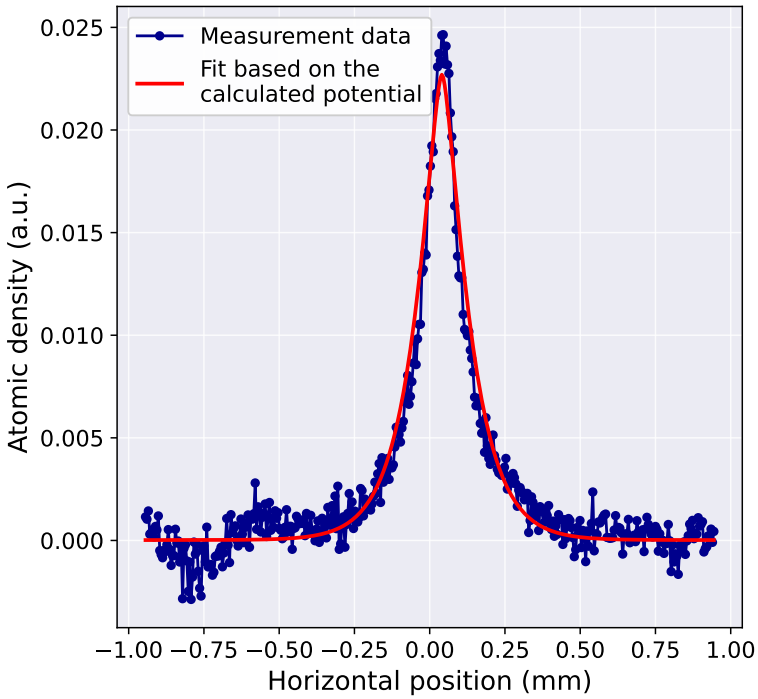

Fig. 3.18: Horizontal density distribution in the magnetic trap.

the cold cloud, meaning that all atoms in the MT have gone through sub-Doppler cooling. Since sub-Doppler cooling is predicated on the fact that the atoms are preferentially excited on the $m_J = +2 \rightarrow m'_J = +3$ transition, it follows that the overwhelming majority of atoms will be in the $m_J = 2$ state, therefore we have assumed $m_J = +2$ across the whole sample. From this fit, we consistently measure magnetic trap temperatures (T_m) between 40 and 60 µK in the magnetic trap, significantly colder than the cold cloud of the MOT T_c. It is of note that $3T_m \approx T_c$ holds consistently in the whole measurement range. The explanation for this phenomenon is grounded in the virial theorem, and the fact that the character of the potential changes when transferring atoms from a(n approximately quadratic) MOT to a linear magnetic trap. As described in [88], assuming the transfer happens in the center of the MOT, with negligible potential energy:

$$\frac{3}{2}k_B T_{MOT} = E_{kin,MOT} = E_{kin,MT} + U_{kin,MT} \tag{3.2}$$

Since in a linear potential ($U_{kin} = 2E_{kin}$):

$$E_{kin,MOT} = 3E_{kin,MT} = 3 \cdot \frac{3}{2} k_B T_{MT} \tag{3.3}$$

So far, the factor three should hold exact for all parameters. If we include in the calculation the effect of the non-zero potential energy of the atoms at the time of the transfer, we need to represent this with a correction factor ΔT, defined as:

$$\Delta T = \frac{8}{9\sqrt{2\pi}} \frac{\mu_b g_J m_J}{k_B} G\sigma \tag{3.4}$$

The results of the comparison between atom temperatures in the magnetic trap measured directly, and those calculated from the above equations are in agreement

with each other within measurement error, and are pictured in Fig. 3.19. This comparison also provides a second, independent way to corroborate our temperature measurements of the magnetic trap and the cold cloud with each other. To our knowledge, this is the the lowest reported temperature of strontium in a magnetic trap.

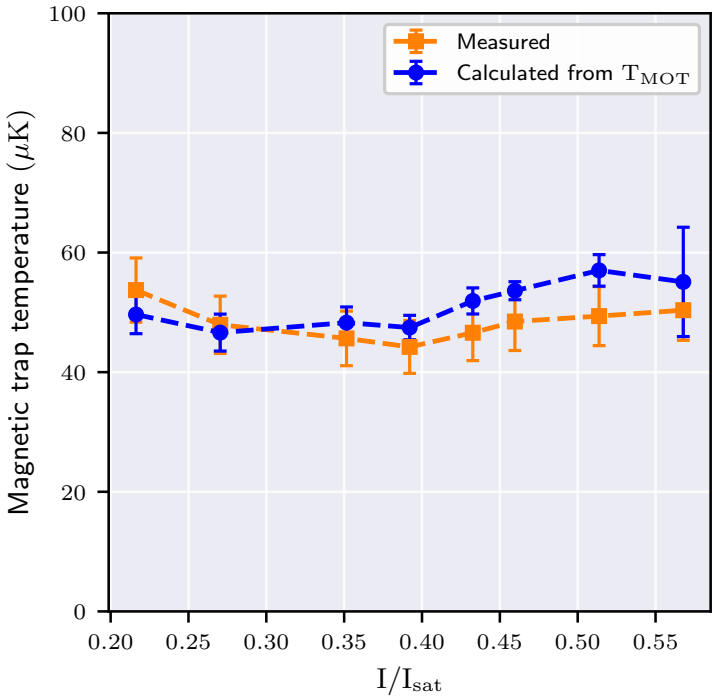

Fig. 3.19: A comparison of the results of two temperature determination methods of the magnetic trap

The atom number or temperature of the warm cloud has no effect on the magnetic trap. We explain this with the fact that the similar atom number to the cold cloud and six to ten times higher temperature results in a much more dilute cloud, which is obscured by the background noise of the measurement. The transfer efficiency from the cold cloud to the magnetic trap is shown in Fig. 3.20a.

We find that the transfer to the magnetic trap occurs with an efficiency constant within measurement error. We measure the lifetime of the atoms in the magnetic trap by determining the population after various holding times and fitting this data with an exponential decay, as shown in Fig. 3.20b, giving us a result of $\tau_{\mathrm{MT}} = 0.53 \pm 0.05$ seconds. As we will see later, the lifetime of the atoms in the dipole trap matches this value. This suggests that the lifetimes are limited by collisions with the background gas or untrapped Sr atoms. Light assisted losses are negligible since the $5s5p^3P_2$ state is dark to all lasers that are on during this measurement. To further corroborate this, a quick estimate about Majorana losses (the other main loss factor in a linear magnetic trap) gives us a lifetime of $\tau_{MT} = 1.26$ seconds;

$$\tau_{Majorana} = \frac{2}{3}\frac{m_{Sr}}{\hbar}\frac{k_B T}{\mu_b m_J g_J G} \tag{3.5}$$

which is significantly higher.

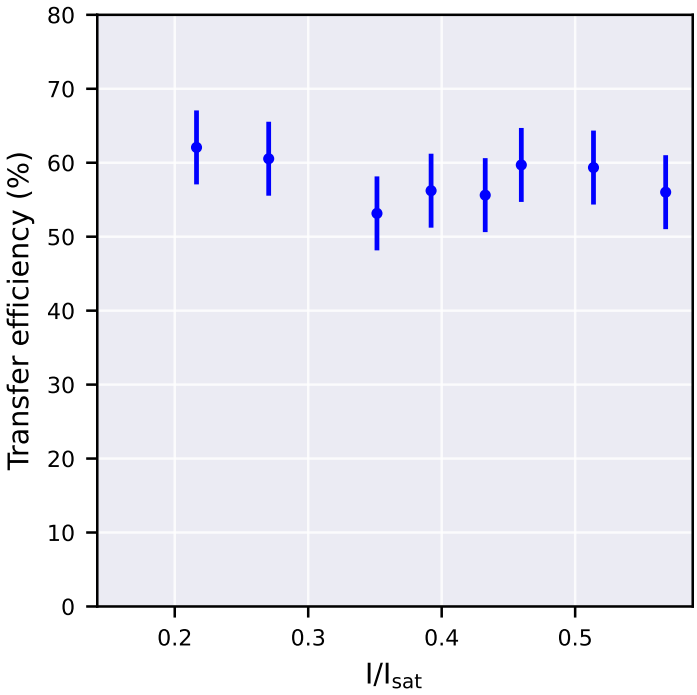

(a) Magnetic trap transfer efficiency

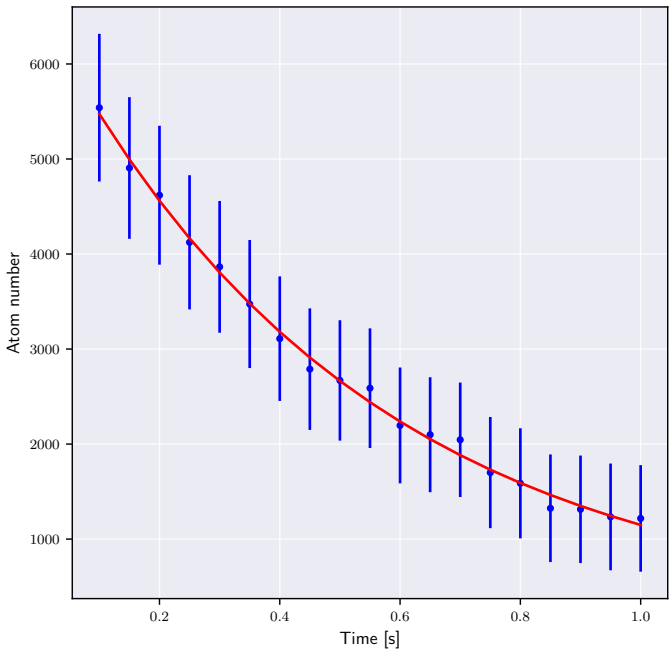

(b) Magnetic trap lifetime

Fig. 3.20: Magnetic trap measurements

3.7 Transferring atoms to the dipole trap

After the characterization of the MOT, our next step was to transfer the atoms to a far off-resonant optical trap. Since the upper state of the green MOT ($5s5d^3D_3$) lies quite high in energy, direct transfer by overlapping the MOT with a magic-wavelength lattice is not possible, as it will ionize atoms in the upper state and the MOT is destroyed. We have measured the MOT fluorescence in the presence of a focused beam overlaid on the MOT depending on the dipole laser wavelength. The beam was focused to a Gaussian beam waist of 30 µm, and we used 15 mW of power, which was generated by a Ti:Sapphire laser (Tekhnoscan TIS-SF-777). A comparison of that measurement to the calculated energy difference between the $5s5d^3D_3$ state and the first ionization energy of Sr is shown in Fig. 3.21.

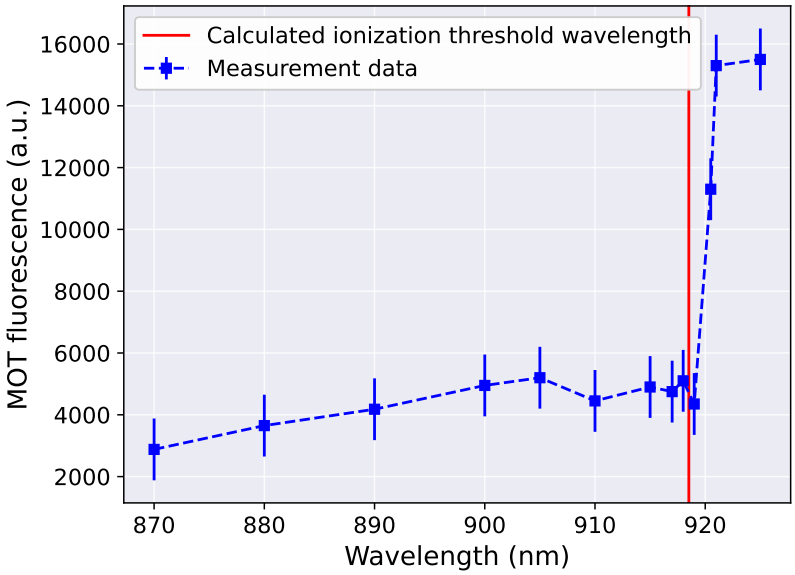

Fig. 3.21: Ionization threshold of the green MOT atoms

Based on this measurement result and hardware availability, a new dipole trap wavelength of 1064 nm was chosen.

The general timing diagram for the dipole trap measurements is shown in Fig. 3.8d. $\Delta t_1 = 5$ ms (the loading time), Δt_2 (the holding time) was varied for the lifetime measurements and was a fixed 20 ms for the temperature and atom number measurements. Δt_3 (the imaging delay time) was varied for the temperature measurements, and was a fixed 100 µs for the lifetime measurements.

We have measured the temperature and number of the atoms in the dipole trap after a holding time of 20 ms. The results are shown in Fig. 3.22. We see that the atom number saturates around 6 W of cooling laser power.

We note that the measured parameters are compatible with recent proposals for continuously operated clocks based on longitudinal Ramsey spectroscopy using ^{88}Sr atoms [89].

We have also measured the lifetime of the atoms in the dipole trap at different trapping powers, the effects of which are shown in Fig. 3.23.

We can observe two distinct decay time scales, with time constants $\tau_1 = 30$ ms to 50 ms and $\tau_2 \approx 600$ ms. The shorter decay is explained by the atoms of the hot cloud leaving the imaging range slowly, because they are "channelled" along the

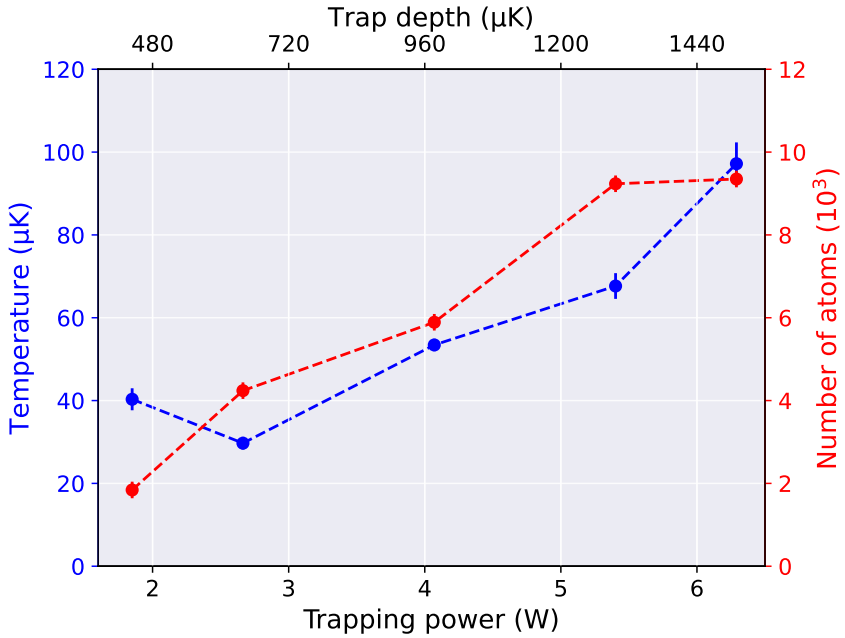

Fig. 3.22: Atom number and temperature depending on dipole trap laser power

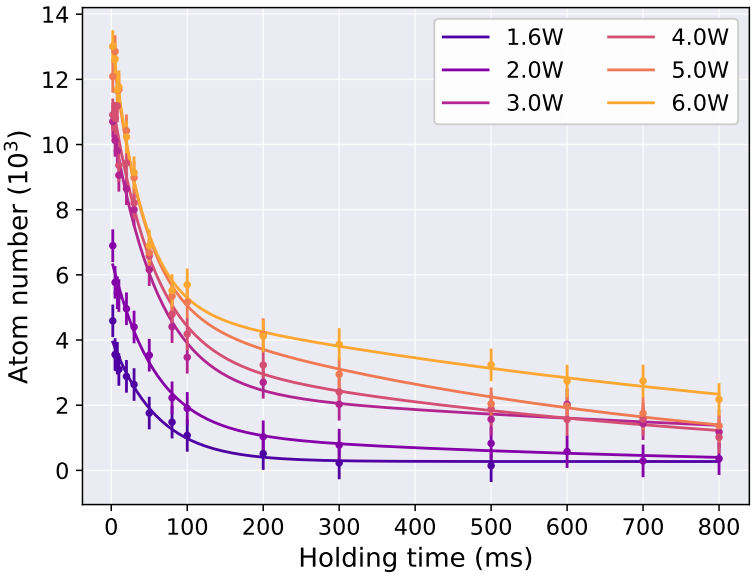

Fig. 3.23: Lifetime of atoms in the dipole trap for different trapping laser intensities

dipole trap potential since it is much more shallow in one direction. The imaging range is $\pm 1\,\mathrm{mm}$, which, assuming atoms with a speed of $30\,\mathrm{cm\,s^{-1}}$ propagating at a five degree angle to the imaging beam, gives us a time of $t_{im} \approx 38\,\mathrm{ms}$ until they pass the border of the range, in good correspondence of the measurement data. The longer scale is the true lifetime of the sub-Doppler cooled atoms from the MOT, and it is in good agreement with the previously measured magnetic trap lifetime, suggesting background gas and Sr collisions being the dominant factor in losses.

"Every so often, you have to unlearn what you thought you already knew, and replace it by something more subtle."

Terry Pratchett, The Science of Discworld

Chapter 4

Sub-doppler cooling

We will now introduce a detailed description of the sub-Doppler cooling process in general and the $\sigma^+ - \sigma^-$ configuration in particular relying on [90] for the general thought process. After that, we will present our calculations conducted regarding the temperature of the MOT, based on the methods laid forth in [91] and [92], adapting them for the Sr atom. Finally, we compare our temperature measurements with the results of these calculations. A detailed account of the theoretical analysis and the calculations will be a subject of future work.

4.1 Sub-Doppler cooling

Both Doppler and sub-Doppler laser cooling methods rely on creating a laser field in which the atoms can only move with their internal state changing non-adiabatically, which means they experience a friction force, losing energy to the field and being cooled by it. For a simple model of the Doppler cooling, where the cooled atomic species is treated as a two-level atom, we can introduce the following nonadiabaticity parameter to characterize the effects: $\epsilon = kv\tau = kv/\gamma$ with τ the lifetime of the upper state. For a single atomic species in a given laser field, smaller values of this parameter correspond to slower atoms which move less during the time a single absorption-stimulated emission cycle takes place, therefore following the field more adiabatically and being cooled less.

Should we desire to explain the process of sub-Doppler cooling, we need to account for the Zeeman sublevels of the ground state (if these do not exist, sub-Doppler cooling is not possible). In the case of a multi-level atom, we need to consider a second relaxation time, τ', which is the average time for an atom to be transferred between sub-levels of the ground state by an absorption-spontaneous emission cycle. This leads to the definition of a second nonadiabaticity parameter $\epsilon' = kv\tau' = kv/\gamma'$. We can see that for the same atom and laser field ϵ' is always greater than ϵ, in the usual regime of small intensities where cooling processes are studied, significantly so ($\gamma' < \gamma \Rightarrow \epsilon' > \epsilon$). This means that for the same v, much higher nonadiabaticity parameters can be achieved, or consequently, much slower atoms can still be affected by the cooling mechanism, lowering the temperature limit of the process in contrast to the two-level atom (or atoms with a nondegenerate ground state).

The nonadiabaticity parameter being in the desired range is alone not enough to provide a high friction force, a strong positional dependence in the anisotropy of the ground state is also required. This is called atomic orientation, and is defined

as a state where $\langle J_k \rangle \neq 0$. Consequently, high differences in the populations of different ground level substates are necessary, and this can be achieved by having some kind of polarization gradient. In the *lin/lin* configuration for example, the polarization changes in one characteristic length from σ^+ to σ^-, meaning that the state $|g, m = J\rangle$ where the atom is getting pumped by the laser radiation is changed to $|g, m' = -J\rangle$.

4.1.1 σ^+ - σ^- configuration

The σ^+ - σ^- cooling configuration consists of two (six in 3D) laser beams of the same intensity, counterpropagating along the axis (z), that have orthogonal, circular polarizations, such that:

$$\boldsymbol{E} = E_0 \boldsymbol{e}^- e^{i(kz-\omega t)} - E_0 \boldsymbol{e}^+ e^{i(kz+\omega t)} + c.c. = E_0 \boldsymbol{e}(z) e^{-i\omega t} + c.c.,$$

where $\boldsymbol{e}^{\pm} = \mp(\boldsymbol{e}_x \pm i\boldsymbol{e}_y)/\sqrt{2}$ and $\boldsymbol{e}(z) = \boldsymbol{e}^- e^{ikz} - \boldsymbol{e}^+ e^{-ikz}$.

The second form shows us that the polarization of the standing wave created by the laser beams is linear in each point, but the plane rotates with a periodicity of λ along the z axis. It is useful to now consider a reference frame which rotates with the same speed as the polarization, and it translates at the same speed as the atom. In this frame, an inertial field will occur according to Larmor's theorem. In its effect, this field will be analogous to a magnetic field that is parallel to the rotation axis (z). The Hamiltonian in this frame will contain a new, inertial term in the form of $V_{rot} = kvJ_z$. It can be shown [90] that this new inertial term introduces a coupling between the ground states that is proportional to kv. This coupling is nonadiabatic (its contribution vanishes when v tends to zero), and will result in an atomic orientation along z.

This atomic orientation has important consequences regarding the behaviour of the atom in the laser field: the states that are populated over the equilibrium possess higher Clebsch-Gordan coefficients compared to the underpopulated ones, which means they are more likely to scatter counterpropagating photons than co-propagating ones by a significant margin. This is the origin of the friction force seen by the atoms in a σ^+ - σ^- sub-Doppler cooling configuration.

4.2 Finding the cooling limit for the green transition

In this section we present two methods that allows for calculating the velocity distribution and thereby the cooling limit for the Sr MOT using the *green* transition, and the approximations taken or neglected for both calculations.

The two methods are termed *semi-classical* and *fully quantum* calculations, but it is important to note that these terms are not used in their usual meaning here, i.e. whether or not the laser fields are take into account in a classic or quantum way. Rather, these terms here refer to the handling of the atom distribution. In the *semi-classical* calculation, the spatial and velocity distribution of the atoms is handled through taking the expectation values of all quantum mechanical variables, in contrast to the fully quantum treatment. Additionally, the semi-classical treatment makes several assumptions detailed below, that limit its applicability regarding certain atoms and transitions.

4.2.1 Semi-classical approach

The semi-classical approach is based on solving the following Fokker-Planck type equation:

$$\frac{p}{M}\frac{\partial}{\partial z}f(z,p) = \left[-\frac{\partial}{\partial p}F(z,p) + \frac{\partial^2}{\partial p^2}D(z,p)\right] f(z,p), \tag{4.1}$$

where $f(z,p)$ is the Wigner distribution function of the atomic ensemble in phase space, M is the atomic mass, $F(z,p)$ is the force from the laser field acting on atoms in z position with p momentum, and the term $D(z,p)$ represents diffusion.

To be able to solve this equation and find the velocity distribution in Sr for the *green* transition, we need to make the following assumptions:

1. $\hbar k/\Delta p \ll 1$: The characteristic width of the final momentum distribution must be significantly larger than momentum delivered to the atom by a single photon scattering event. Since Δp is not known in advance, this makes it difficult to predict if this assumption will be fulfilled in a given case.

2. $t_r \gg \gamma S$: The relaxation time of the internal atomic state must be much longer than the characteristic pumping time between magnetic ground substates.

3. $\omega_r \ll \gamma S$: The recoil frequency needs to be much smaller than the characteristic optical pumping rate between substates.

S is defined as:

$$S \equiv \frac{R^2}{(\gamma/2)^2 + \delta^2},$$

where R is the Rabi frequency: $R = dE_0/\hbar$. Additionally, the *Rotating Wave Approximation (RWA)* will also be used in this calculation method.

The light force term in Eq. (4.1) is defined as $F(z,p) = Tr\left\{\hat{F}(z)\hat{\rho}^{(0)}(z,p)\right\}$, with $\hat{F}_z = -\frac{\partial}{\partial}\hat{V}(z)$. It is important to note that $\hat{p}^{(n)}$ will denote the n-th order expansion of the density matrix in the variable $\hbar k$ during this calculation. This is where approximation 1 plays a rule, allowing us to do this. The $\hat{V}$ operator does not depend on time (since we are using the RWA approximation, therefore $\hat{V} = -dE_0\hat{V}^{eg}(z) + h.c.$, with d being the usual reduced dipole matrix element, and

$$\hat{V}^{eg} = \sum_{q,m_q,m_e} e_q(z) C^{J_e,m_e}_{J_g,m_g;1,q} |F_e, m_e\rangle\langle F_g, m_g|.$$

F_g and F_e are the total angular momenta of the ground and excited states, $q = \{-,+\}$ and $m_a = -F_a ... F_a$. The diffusion term can be divided into two parts: $D(z,p) = D_s(z,p) + D_i(z,p)$ where D_s describes the fluctuation of the direction of the photons emitted through spontaneous emission, and D_i describes fluctuations in the light force, such that:

$$D_s = \frac{\gamma(\hbar k)^2}{5} Tr\left\{\left(\hat{P}_e - \frac{1}{2}\hat{T}_0\hat{T}_0^\dagger\right)\hat{\rho}^{(0)}(z,p)\right\},$$

and

$$D_i = Tr\left\{\hat{F}(z)\hat{\rho}^{(1)}(z,p)\right\}.$$

In these terms, $\hat{P}_e = |F_e, m_e\rangle\langle F_e, m_e|$, and $\hat{T}_0 = \hat{T} \cdot e_z$ is

$$\hat{\boldsymbol{T}} = \sum_{q,m_e,m_g} \boldsymbol{e}_q C^{F_e,m_e}_{F_g,m_g;1,q} |F_e, m_e\rangle\langle F_g, m_g|.$$

$\hat{\rho}^{(0)}$ in the steady state is described by

$$\frac{p}{M}\frac{\partial}{\partial z}\hat{\rho}_0 + \frac{i}{\hbar}\left[\left(-\hbar\delta\hat{P}_e + \hat{V}\right), \hat{\rho}^{(0)}\right] + \hat{\Gamma}\left\{\hat{\rho}^{(0)}\right\} = 0.$$

The $\hat{\Gamma}$ operator accounts for spontaneous relaxation:

$$\hat{\Gamma} = \frac{\gamma}{2}\left\{\hat{P}^e, \hat{\rho}^{(0)}\right\} - \gamma \sum_{q=0,\pm1} \hat{T}_q^\dagger \hat{\rho}^{(0)} \hat{T}_q.$$

In addition, the normalization condition $Tr\left\{\hat{\rho}^{(0)}\right\} = 1$ has to be fulfilled.

While calculating the σ^+ - σ^- configuration, the equations can be significantly simplified by using the rotating coordinate system described in Subs. 4.1.1. This results in the entire problem losing its spatial dependence, thereby making the solution numerically much less demanding. For details of this transformation and the numerical solutions, as calculated on another atomic species, the reader is referred to [91].

We briefly call attention here to the limitations of the semiclassical method. In the low intensity regime especially, many actual velocity distributions do not fulfill the requirement for assumption 1 of the semiclassical approximation. The green MOT in Sr is also in this group. In such cases, the semi-classical approximation tends to significantly underestimate the achievable minimum average velocity especially in the low saturation regime, where the our MOT produces the best results regarding the minimum temperature of the cold cloud.

4.2.2 Full quantum treatment

Keeping the light field the same as in the previous calculation, the full quantum treatment starts with a single-atom density matrix, which we will use in two-point coordinate representation [92]. The semiclassical approximations from the previous section are no longer valid, but the RWA still remains in effect. The equation we want to solve takes the following form in this representation:

$$\frac{\partial\hat{\rho}(z_1, z_2, t)}{\partial t} = -\frac{i}{\hbar}\left[\hat{H}(z_1, t)\hat{\rho} - \hat{\rho}\hat{H}(z_2, t)\right] + \hat{\Gamma}\left\{\hat{\rho}\right\}. \tag{4.2}$$

The Hamiltonians are

$$\hat{H}(z_i, t) = \frac{\hat{p}_i^2}{2M} + \hat{H}_0 + \hat{V}(z_i, t).$$

Using the definitions of the $\hat{P}_e$ projection operator and $\hat{\boldsymbol{T}}$ Wigner vector operator from the previous chapter, the terms of the Hamiltonian can be rewritten as:

$$\hat{H}_0 = -\hbar\delta\hat{P}_e \text{ and } \hat{V}(z_i) = E_0 d\hat{V}^{eg}(z_i) + h.c..$$

We now transform into a new coordinate basis with the dimensionless $z = k(z_1 + z_2)/2$ and $q = k(z_1 - z_2)$ as the new coordinates. In this basis, the $\hat{\Gamma}$ operator functional has the following form:

$$\hat{\Gamma} = \frac{\gamma}{2}\left(\hat{P}^e\hat{\rho} + \hat{\rho}\hat{P}^e\right) + \gamma \sum_{\sigma=0,\pm1} \zeta_\sigma(q)\hat{T}_q^\dagger\hat{\rho}\hat{T}_q,$$

where

$$\zeta_{\pm1} = \frac{3}{2}\left[\frac{\sin(q)}{q} - \frac{\sin(q)}{q^3} + \frac{\cos(q)}{q^2}\right],$$

and

$$\zeta_0 = \left[\frac{\sin(q)}{q^3} - \frac{\cos(q)}{q^2}\right]$$

Let us take a look at the structure of the density matrix:

$$\hat{\rho} = \begin{pmatrix} \hat{\rho}^{gg} & \hat{\rho}^{ge} \\ \hat{\rho}^{eg} & \hat{\rho}^{ee} \end{pmatrix}$$

The blocks in the main diagonal describe the populations of the ground and excited substates, and the others the optical coherences between them.

Applying everything up to now, in steady state the following equation system emerges:

$$-2i\omega_r\frac{\partial^2}{\partial q\partial z}\hat{\rho}^{gg}(z,q) = \gamma \sum_{\sigma=0,\pm1} \zeta_\sigma(q)\hat{T}_q^\dagger\hat{\rho}^{(0)}\hat{T}_q + \tag{4.3}$$

$$iR\left[\hat{V}^{eg\dagger}\left(z+\frac{q}{2}\right)\hat{\rho}^{eg} - \hat{\rho}^{ge}\hat{V}^{eg}\left(z-\frac{q}{2}\right)\right]$$

$$\left(\gamma - 2i\omega_r\frac{\partial^2}{\partial q\partial z}\right)\hat{\rho}^{ee}(z,q) = iR\left[\hat{V}^{eg}\left(z+\frac{q}{2}\right)\hat{\rho}^{ge} - \hat{\rho}^{eg}\hat{V}^{eg\dagger}\left(z-\frac{q}{2}\right)\right] \tag{4.4}$$

$$\left(\frac{\gamma}{2} + i\delta - 2i\omega_r\frac{\partial^2}{\partial q\partial z}\right)\hat{\rho}^{ge}(z,q) = iR\left[\hat{V}^{eg\dagger}\left(z+\frac{q}{2}\right)\hat{\rho}^{ee} - \hat{\rho}^{gg}\hat{V}^{eg\dagger}\left(z-\frac{q}{2}\right)\right] \tag{4.5}$$

$$\left(\frac{\gamma}{2} - i\delta - 2i\omega_r\frac{\partial^2}{\partial q\partial z}\right)\hat{\rho}^{eg}(z,q) = iR\left[\hat{V}^{eg}\left(z+\frac{q}{2}\right)\hat{\rho}^{gg} - \hat{\rho}^{ee}\hat{V}^{eg}\left(z-\frac{q}{2}\right)\right], \tag{4.6}$$

The velocity distribution can be calculated according to:

$$f(p) = \frac{1}{(2\pi)^2}\int_{-\infty}^{\infty} dq \int_{-\pi}^{\pi} dz \mathrm{Tr}\left\{\hat{\rho}(z,q)\right\} e^{-ipq}, \tag{4.7}$$

with the additional norming condition: $\int_{-\infty}^{\infty} f(p) = 1$

In a σ^+ - σ^- configuration, in the rotating coordinate system, the z-dependence is not present anywhere in the equation system, significantly reducing the numerical load when solving it. With the proper coordinate transformation [92], the above equation system takes the following form:

$$2\omega_r\frac{\partial}{\partial q}\left[\hat{J}_z, \hat{\rho}(q)\right] = \hat{\Gamma}\left\{\hat{\rho}(q)\right\} + i\delta\left[\hat{P}^e, \hat{\rho}\right] + i\Omega\left[\hat{V}_1(q)\hat{\rho} - \hat{\rho}\hat{V}_2(q)\right], \tag{4.8}$$

And the normalization condition also simplifies to $\mathrm{Tr}\{\hat{\rho}(q=0)\} = 1$.

Numerically solving the equations, we get the following curve for the minimum effective temperature plotted against the saturation parameter. We have included the results of the semiclassical calculation on in the same figure, to illustrate its effect of underestimating the temperature limit. All calculations and measurements were done with a detuning of $\delta = 19\mathrm{MHz}$.

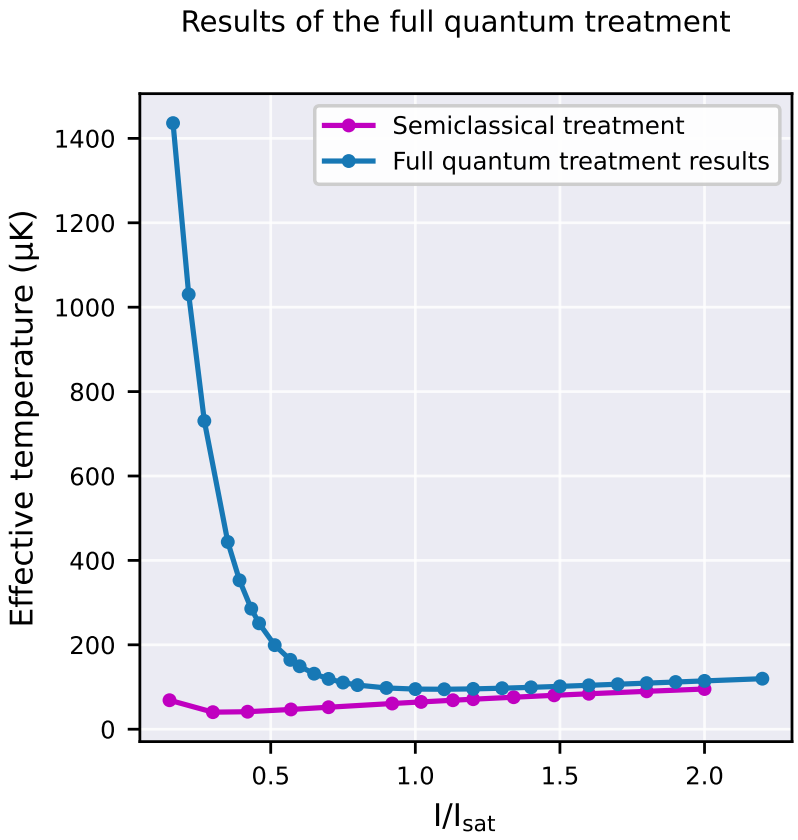

Fig. 4.1: The effective temperature limit of the strontium green transition as a function of the saturation parameter calculated semiclassically and with a full quantum treatment

In Fig. 4.2 we see the comparison of our measurement data with the results of the full quantum calculation. For the lower saturation parameters, the measured data show good agreement with the predictions, but plateaus at a significantly higher temperature than the theoretical results.

A partial reason for the discrepancy can be found by considering the fact that our calculation so far only considered cooling in a molasses. While this is useful for a first approximation, the quadrupole magnetic field of the MOT has a significant effect on the temperature limit, as we will demonstrate.

To include the effect of the magnetic field, we need to make the following adjustments to the original Eq. (4.7): We have to include an extra interaction term to the right side of the equation, in the form of:

$$\hat{H}_z \equiv i\mu_B \frac{G}{k}\left((z+\frac{q}{2})\hat{O}\hat{\rho}(z,q) - (z-\frac{q}{2})\hat{\rho}(z,q)\hat{O}\right).$$

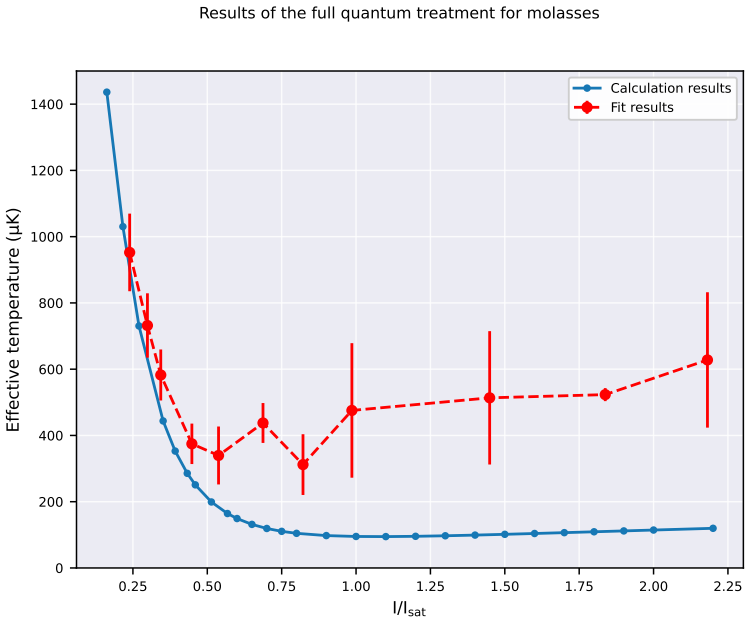

Fig. 4.2: The results of the full quantum treatment compared with our measurement data

Where

$$\hat{O} \equiv \begin{bmatrix} g_{J,e} - J_e & & & & & & & & \\ & g_{J,e}(-J_e+1) & & & & & & & \\ & & \ddots & & & & & & \\ & & & g_{J,e}(J_e-1) & & & & & \\ & & & & g_{J,e}(J_e) & & & & \\ & & & & & g_{J,g}(-J_g) & & & \\ & & & & & & \ddots & & \\ & & & & & & & g_{J,g}(J_g) \end{bmatrix}. \tag{4.9}$$

Unfortunately, since the system is no longer z independent, we boundary condition reverts to the original $\frac{1}{2\pi}\int_{-\pi}^{\pi} dz\ \mathrm{Tr}\,\hat{\rho}(z, q=0) = 1$. This makes the calculation impossible for any feasible parameter grid, therefore we need to make an approximation similar to that used in [93]: We solve the equation for a fixed z setting $q = 0$ into the Zeeman-term, and return to the simplified boundary condition of $\mathrm{Tr}\,\{\hat{\rho}(q=0)\} = 1$. After calculating the momentum distribution for given z parameters, we average them together using the (experimentally detected) MOT density distribution as a weight function, obtaining the final momentum distribution.

As we can see in Fig. 4.3, the plateau of the effective temperature occurs at a significantly higher temperature than the calculation without a Zeeman term. For high intensities the measured temperatures are still higher than the calculation. Because of the z-dependence in the full quantum treatment with a magnetic field, our solution is necessarily an approximation. Since the optimal density and temperature of the cold inner cloud are in a MOT with a saturation parameter between 0.25-0.5 (as shown in Fig. 3.13) where the model already shows good agreement with our measurements, the discrepancy in higher intensities was not pursued further.

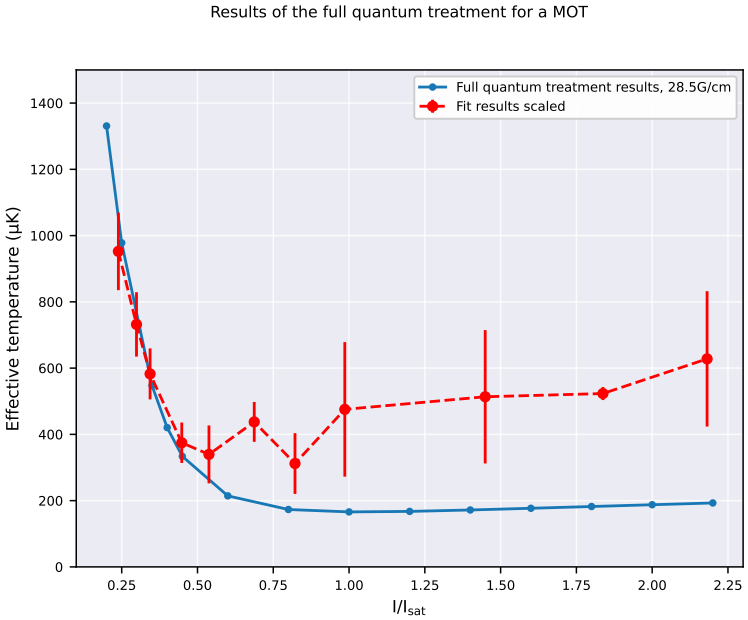

Fig. 4.3: The results of the full quantum treatment including a Zeeman term when compared with our measurement data

"The prudent text-books give it
In tables at the end–
The stress that shears a rivet
Or makes a tie-bar bend—
What traffic wrecks macadam—
What concrete should endure—
But we, poor Sons of Adam
Have no such literature,
To warn us or make sure!"

Rudyard Kipling, Hymn of Breaking Strain

Chapter 5

Conclusion

Precision time metrology is as much a building block of our lives today as it was throughout the centuries. It not only promises results in fundamental science, but also everyday applications that we might encounter sooner rather than later.

To further this scientific field, we have presented our work laying the basis of an interruption-free frequency standard, which would significantly lower the limits of neutral atomic clock precision. We have built and characterized a system that is capable of producing a two-color continuous magneto-optical trap of Sr atoms, and demonstrated the transfer of these atoms to a dipole trap, as a precursor for continuous extraction with a moving lattice. Additionally, we have calculated the theoretical limits of the sub-Doppler cooling exhibited by the second cooling cycle of the MOT, and we have found good agreement between the results of this calculation and our measurement data. To our knowledge, this specific calculation and comparison for a $J = 2 \rightarrow J' = 3$ transition in Sr was not published before.

We have also demonstrated that the dual structure of such a MOT makes it possible to extract atoms preferentially from the sub-Doppler cooled cloud, achieving temperatures below 120 µK, in spite of average effective temperatures over 300 µK. The high atomix flux of sub-Doppler cooled atoms offers interesting future possibilites of extracting atoms with shallow optical lattices, or additional cooling after the extraction, to facilitate interruption-free spectroscopy of Sr atoms.

Acknowledgement

First and foremost, I would like to give my thanks to my beautiful and kind wife Réka, without whom this dissertation would not exist, and neither would what little remains of my sanity.

I would like to extend my thanks to Lőrinc Sárkány for his continuous support and mentorship, and for always teaching me new things not limited to physics, and to József Fortágh, for recruiting me to his group and giving me the opportunity to work at the cutting edge of research. Also many thanks to Shubha Deutschle for all the fun times we spent working in the lab.

I would like to thank Christian Groß as well for his many helpful suggestions concerning our measurement system, as well as for loaning us the dipole trap laser.

My thanks belong with the mechanical workshop of the university led by Norbert Stockmaier as well. Without them, our experiment would have never gotten to the state it is in today.

Pictures illustrating optical arrangements were created using ComponentLibrary, created by Alexander Franzen, licenced under Creative Commons Attribution-NonCommercial 3.0 Unported License.

https://www.gwoptics.org/ComponentLibrary/

https://creativecommons.org/licenses/by-nc/3.0/

Declaration of contributions

When I joined the project there has been a setup by L. Sárkány and F. Jessen operating a blue Sr MOT [76, 77]. In collaboration with S. Deutschle, I extended the setup by a laser system for the green MOT, collected the measurement data, and performed data analysis. The theoretical description has been created by L. Sárkány; he also assisted in evaluating the measurement data.

A publication representing the key results has been prepared and submitted to the journal Physical Review A. The manuscript is already available on the preprint platform arXiv under the title "Sub-Doppler cooling of bosonic strontium in a two-color MOT" (https://doi.org/10.48550/arXiv.2507.02693).

Bibliography

[1] William J. H. Andrewes. "A chronicle of timekeeping". In: *Scientific American* 287 3 (2002), pp. 76–85.

[2] J. Jackson. "Shortt Clocks and the Earth's Rotation". In: *Monthly Notices of the Royal Astronomical Society* 89.3 (Jan. 1929), pp. 239–250.

[3] BIPM. *Le Système international d'unités / The International System of Units ('The SI Brochure')*. Ninth. Bureau international des poids et mesures, 2019.

[4] William Thomson Kelvin and Peter Guthrie Tait. *Treatise on natural philosophy*. University Press, Cambridge, 1879.

[5] H. G. Dehmelt. In: *Bull. Am. Phys. Soc.* 18 (1973), p. 1521.

[6] *Longitude found: the story of Harrison's clocks*. URL: https://www.rmg.co.uk/stories/topics/harrisons-clocks-longitude-problem (visited on 03/15/2023).

[7] Michael Lombardi, Thomas Heavner, and Steven Jefferts. "NIST Primary Frequency Standards and the Realization of the SI Second". en. In: 2 (Dec. 2007).

[8] Masao Takamoto et al. "An optical lattice clock". In: *Nature* 435.7040 (May 2005), pp. 321–324.

[9] Christopher J. Hegarty. "The Global Positioning System (GPS)". In: *Springer Handbook of Global Navigation Satellite Systems*. Ed. by Peter J.G. Teunissen and Oliver Montenbruck. Cham: Springer International Publishing, 2017, pp. 197–218.

[10] Sergey Revnivykh et al. "GLONASS". In: *Springer Handbook of Global Navigation Satellite Systems*. Ed. by Peter J.G. Teunissen and Oliver Montenbruck. Cham: Springer International Publishing, 2017, pp. 219–245.

[11] Marco Falcone, Jörg Hahn, and Thomas Burger. "Galileo". In: *Springer Handbook of Global Navigation Satellite Systems*. Ed. by Peter J.G. Teunissen and Oliver Montenbruck. Cham: Springer International Publishing, 2017, pp. 247–272.

[12] Yuanxi Yang, Jing Tang, and Oliver Montenbruck. "Chinese Navigation Satellite Systems". In: *Springer Handbook of Global Navigation Satellite Systems*. Ed. by Peter J.G. Teunissen and Oliver Montenbruck. Cham: Springer International Publishing, 2017, pp. 273–304.

[13] Satoshi Kogure, A.S. Ganeshan, and Oliver Montenbruck. "Regional Systems". In: *Springer Handbook of Global Navigation Satellite Systems*. Ed. by Peter J.G. Teunissen and Oliver Montenbruck. Cham: Springer International Publishing, 2017, pp. 305–337.

[14] Richard B. Langley, Peter J.G. Teunissen, and Oliver Montenbruck. "Introduction to GNSS". In: *Springer Handbook of Global Navigation Satellite Systems*. Ed. by Peter J.G. Teunissen and Oliver Montenbruck. Cham: Springer International Publishing, 2017, pp. 3–23.

[15] William Loh et al. "Operation of an optical atomic clock with a Brillouin laser subsystem". In: *Nature* 588.7837 (Dec. 2020), pp. 244–249.

[16] E. A. Burt et al. "Demonstration of a trapped-ion atomic clock in space". In: *Nature* 595.7865 (July 2021), pp. 43–47.

[17] Benjamin W. Ashman et al. "Exploring the Limits of High Altitude GPS for Future Lunar Missions". In: 2018.

[18] Luke B. Winternitz et al. "GPS Based Autonomous Navigation Study for the Lunar Gateway". In: 2019.

[19] *NSN Service Brochure*. URL: https://esc.gsfc.nasa.gov/static-files/NSN%20Services%20Brochure.pdf (visited on 03/15/2023).

[20] Anaïs Delépaut et al. "Use of GNSS for lunar missions and plans for lunar in-orbit development". In: *Advances in Space Research* 66.12 (2020). Scientific and Fundamental Aspects of GNSS - Part 1, pp. 2739–2756.

[21] Masao Takamoto et al. "Test of general relativity by a pair of transportable optical lattice clocks". In: *Nature Photonics* 14.7 (July 2020), pp. 411–415.

[22] Tobias Bothwell et al. "Resolving the gravitational redshift across a millimetre-scale atomic sample". en. In: *Nature* 602.7897 (Feb. 2022), pp. 420–424.

[23] Tanja E Mehlstäubler et al. "Atomic clocks for geodesy". In: *Reports on Progress in Physics* 81.6 (Apr. 2018), p. 064401.

[24] Yoshiyuki Tanaka and Hidetoshi Katori. "Exploring potential applications of optical lattice clocks in a plate subduction zone". In: *Journal of Geodesy* 95.8 (July 2021), p. 93.

[25] Ruxandra Bondarescu et al. "Ground-based optical atomic clocks as a tool to monitor vertical surface motion". In: *Geophysical Journal International* 202.3 (July 2015), pp. 1770–1774.

[26] The Event Horizon Telescope Collaboration et al. "First M87 Event Horizon Telescope Results. IV. Imaging the Central Supermassive Black Hole". In: *The Astrophysical Journal Letters* 875.1 (Apr. 2019), p. L4.

[27] Cecilia Clivati et al. "A VLBI experiment using a remote atomic clock via a coherent fibre link". In: *Scientific Reports* 7.1 (Feb. 2017), p. 40992.

[28] C. Clivati et al. "Coherent Optical-Fiber Link Across Italy and France". In: *Phys. Rev. Appl.* 18 (5 Nov. 2022), p. 054009.

[29] K. Predehl et al. "A 920-Kilometer Optical Fiber Link for Frequency Metrology at the 19th Decimal Place". In: *Science* 336.6080 (2012), pp. 441–444.

[30] Nicola Chiodo et al. "Cascaded optical fiber link using the internet network for remote clocks comparison". In: *Opt. Express* 23.26 (Dec. 2015), pp. 33927–33937.

[31] P. Delva et al. "Test of Special Relativity Using a Fiber Network of Optical Clocks". In: *Phys. Rev. Lett.* 118 (22 June 2017), p. 221102.

[32] J Guéna et al. “First international comparison of fountain primary frequency standards via a long distance optical fiber link”. In: *Metrologia* 54.3 (May 2017), p. 348.

[33] Cecilia Clivati et al. “Common-clock very long baseline interferometry using a coherent optical fiber link”. In: *Optica* 7.8 (Aug. 2020), pp. 1031–1037.

[34] Colin J. Kennedy et al. “Precision Metrology Meets Cosmology: Improved Constraints on Ultralight Dark Matter from Atom-Cavity Frequency Comparisons”. In: *Phys. Rev. Lett.* 125 (20 Nov. 2020), p. 201302.

[35] Takumi Kobayashi et al. “Search for Ultralight Dark Matter from Long-Term Frequency Comparisons of Optical and Microwave Atomic Clocks”. In: *Phys. Rev. Lett.* 129 (24 Dec. 2022), p. 241301.

[36] V. A. Dzuba, V. V. Flambaum, and S. Schiller. “Testing physics beyond the standard model through additional clock transitions in neutral ytterbium”. In: *Phys. Rev. A* 98 (2 Aug. 2018), p. 022501.

[37] Marianna S. Safronova et al. “Two Clock Transitions in Neutral Yb for the Highest Sensitivity to Variations of the Fine-Structure Constant”. In: *Phys. Rev. Lett.* 120 (17 Apr. 2018), p. 173001.

[38] Fritz Riehle. *Frequency standards: Basics and applications*. Weinheim: Wiley-WCH, 2003.

[39] *International vocabulary of metrology - Basic and general concepts and associated terms (VIM)*. https://jcgm.bipm.org/vim/en/index.html. Accessed: 2023-01-25.

[40] D.W. Allan. “Statistics of atomic frequency standards”. In: *Proceedings of the IEEE* 54.2 (1966), pp. 221–230.

[41] Andreas Bauch. “Caesium atomic clocks: function, performance and applications”. In: *Measurement Science and Technology* 14.8 (June 2003), p. 1159.

[42] Thomas P Heavner et al. “First accuracy evaluation of NIST-F2”. In: *Metrologia* 51.3 (May 2014), p. 174.

[43] Andrew D. Ludlow et al. “Optical atomic clocks”. In: *Rev. Mod. Phys.* 87 (2 June 2015), pp. 637–701.

[44] W. M. Itano et al. “Quantum projection noise: Population fluctuations in two-level systems”. In: *Phys. Rev. A* 47 (5 May 1993), pp. 3554–3570.

[45] Hidetoshi Katori et al. “Magic Wavelength to Make Optical Lattice Clocks Insensitive to Atomic Motion”. In: *Phys. Rev. Lett.* 103 (15 Oct. 2009), p. 153004.

[46] G John Dick. “Local oscillator induced instabilities in trapped ion frequency standards”. In: *Proceedings of the 19th Annual Precise Time and Time Interval Systems and Applications Meeting*. 1989, pp. 133–147.

[47] T. Kessler et al. “A sub-40-mHz-linewidth laser based on a silicon single-crystal optical cavity”. In: *Nature Photonics* 6.10 (Oct. 2012), pp. 687–692.

[48] Johannes Dickmann et al. “Experimental realization of a 12,000-finesse laser cavity based on a low-noise microstructured mirror”. In: *Communications Physics* 6.1 (Jan. 2023), p. 16.

[49] Audrey Quessada et al. "The Dick effect for an optical frequency standard". In: *Journal of Optics B: Quantum and Semiclassical Optics* 5.2 (Apr. 2003), S150.

[50] M. Schioppo et al. "Ultrastable optical clock with two cold-atom ensembles". In: *Nature Photonics* 11.1 (Jan. 2017), pp. 48–52.

[51] Jérôme Lodewyck, Philip G. Westergaard, and Pierre Lemonde. "Nondestructive measurement of the transition probability in a Sr optical lattice clock". In: *Phys. Rev. A* 79 (6 June 2009), p. 061401.

[52] C-C Chen et al. "An atomic marble run to unity phase-space density". In: (2019).

[53] Jeongwon Lee et al. "Core-shell magneto-optical trap for alkaline-earth-metal-like atoms". In: *Phys. Rev. A* 91 (5 May 2015), p. 053405.

[54] Akio Kawasaki et al. "Two-color magneto-optical trap with small magnetic field for ytterbium". In: *Journal of Physics B: Atomic, Molecular and Optical Physics* 48.15 (June 2015), p. 155302.

[55] H.J. Metcalf and P. Van der Straten. *Laser Cooling and Trapping*. Graduate texts in contemporary physics. Springer, 1999.

[56] T.W. Hänsch and A.L. Schawlow. "Cooling of gases by laser radiation". In: *Optics Communications* 13.1 (1975), pp. 68–69.

[57] T. H. MAIMAN. "Stimulated Optical Radiation in Ruby". In: *Nature* 187.4736 (Aug. 1960), pp. 493–494.

[58] J. Fortagh et al. "Fast loading of a magneto-optical trap from a pulsed thermal source". In: *Journal of Applied Physics* 84.12 (Dec. 1998), pp. 6499–6501.

[59] M Zhu, C W Oates, and J L Hall. "Continuous high-flux monovelocity atomic beam based on a broadband laser-cooling technique". In: *Physical Review Letters; (USA)* (July 1991).

[60] R. N. Watts and C. E. Wieman. "Manipulating atomic velocities using diode lasers". In: *Opt. Lett.* 11.5 (May 1986), pp. 291–293.

[61] William D. Phillips and Harold Metcalf. "Laser Deceleration of an Atomic Beam". In: *Phys. Rev. Lett.* 48 (9 Mar. 1982), pp. 596–599.

[62] Hendrick L. Bethlem, Giel Berden, and Gerard Meijer. "Decelerating Neutral Dipolar Molecules". In: *Phys. Rev. Lett.* 83 (8 Aug. 1999), pp. 1558–1561.

[63] Yuri B. Ovchinnikov. "A Zeeman slower based on magnetic dipoles". In: *Optics Communications* 276.2 (2007), pp. 261–267.

[64] Masami Yasuda and Hidetoshi Katori. "Lifetime Measurement of the $^3P_2$ Metastable State of Strontium Atoms". In: *Phys. Rev. Lett.* 92 (15 Apr. 2004), p. 153004.

[65] Fachao Hu et al. "Analyzing a single-laser repumping scheme for efficient loading of a strontium magneto-optical trap". In: *Phys. Rev. A* 99 (3 Mar. 2019), p. 033422.

[66] P G Mickelson et al. "Repumping and spectroscopy of laser-cooled Sr atoms using the (5s5p)3P2–(5s4d)3D2 transition". In: *Journal of Physics B: Atomic, Molecular and Optical Physics* 42.23 (Nov. 2009), p. 235001.

[67] Simon Stellmer and Florian Schreck. "Reservoir spectroscopy of $5s5p\ ^3P_2$–$5snd\ ^3D_{1,2,3}$ transitions in strontium". In: *Phys. Rev. A* 90 (2 Aug. 2014), p. 022512.

[68] Hidetoshi Katori et al. "Magneto-Optical Trapping and Cooling of Strontium Atoms down to the Photon Recoil Temperature". In: *Phys. Rev. Lett.* 82 (6 Feb. 1999), pp. 1116–1119.

[69] Shayne Bennetts et al. "Steady-State Magneto-Optical Trap with 100-Fold Improved Phase-Space Density". In: *Phys. Rev. Lett.* 119 (22 Dec. 2017), p. 223202.

[70] Vladimir Schkolnik, Oliver Fartmann, and Markus Krutzik. "An extended-cavity diode laser at 497 nm for laser cooling and trapping of neutral strontium". In: *Laser Physics* 29.3 (Feb. 2019), p. 035802.

[71] Tomoya Akatsuka et al. "Three-stage laser cooling of Sr atoms using the $5s5p^3P_2$ metastable state below Doppler temperatures". In: *Phys. Rev. A* 103 (2 Feb. 2021), p. 023331.

[72] Yusuke Hayakawa et al. "Doppler-free spectroscopy of metastable Sr atoms using a hollow cathode lamp". In: *Appl. Opt.* 57.6 (Feb. 2018), pp. 1450–1454.

[73] R. Hobson et al. "Midinfrared magneto-optical trap of metastable strontium for an optical lattice clock". In: *Phys. Rev. A* 101 (1 Jan. 2020), p. 013420.

[74] Wolfgang Petrich et al. "Stable, Tightly Confining Magnetic Trap for Evaporative Cooling of Neutral Atoms". In: *Phys. Rev. Lett.* 74 (17 Apr. 1995), pp. 3352–3355.

[75] Milán János Negyedi et al. "Sub-Doppler cooling of bosonic strontium in a two-color MOT". In: *arXiv preprint arXiv:2507.02693* (2025). submitted to Phys. Rev. A.

[76] Lőrinc Sárkány. "Engineering quantum systems for information processing and metrology using atoms, superconductors, and light". Doctoral dissertation. University of Tübingen, 2018.

[77] Florian Jessen. "Entwicklung und Aufbau hybrider Quantensysteme für Quantencomputing und Metrologie". Doctoral dissertation. University of Tübingen, 2018.

[78] Sárkány Lőrinc (DE) Fortágh József (DE) Jessen Florian (DE). "Magnetooptische Falle mit sich partiell kompensierenden Magnetfeldern, insbesondere als kontinuierliche Kaltatomquelle." DE102020117541. Nov. 2021.

[79] Robert Powel et al. "Improved wavelength meter calibration in near infrared region via Doppler-free spectroscopy of molecular iodine". In: *Applied Physics B* 127.7 (June 2021), p. 104.

[80] Kristian König et al. "On the performance of wavelength meters: Part 2—frequency-comb based characterization for more accurate absolute wavelength determinations". In: *Applied Physics B* 126.5 (Apr. 2020), p. 86.

[81] C. F. Ockeloen et al. "Detection of small atom numbers through image processing". In: *Phys. Rev. A* 82 (6 Dec. 2010), p. 061606.

[82] E. Kalganova et al. "Two-temperature momentum distribution in a thulium magneto-optical trap". In: *Phys. Rev. A* 96 (3 Sept. 2017), p. 033418.

[83] Kihwan Kim et al. “Direct observation of the sub-Doppler trap in a parametrically driven magneto-optical trap”. In: *Phys. Rev. A* 69 (3 Mar. 2004), p. 033406.

[84] Seo Ho Youn, Mingwu Lu, and Benjamin L. Lev. “Anisotropic sub-Doppler laser cooling in dysprosium magneto-optical traps”. In: *Phys. Rev. A* 82 (4 Oct. 2010), p. 043403.

[85] Dirk P. Hansen, Janis R. Mohr, and Andreas Hemmerich. “Magnetic trapping of metastable calcium atoms”. In: *Phys. Rev. A* 67 (2 Feb. 2003), p. 021401.

[86] Xinye Xu et al. “Cooling and trapping of atomic strontium”. In: *J. Opt. Soc. Am. B* 20.5 (May 2003), pp. 968–976.

[87] S. B. Nagel et al. “Magnetic trapping of metastable $^3P_2$ atomic strontium”. In: *Phys. Rev. A* 67 (1 Jan. 2003), p. 011401.

[88] J. Stuhler et al. “Continuous loading of a magnetic trap”. In: *Phys. Rev. A* 64 (3 Aug. 2001), p. 031405.

[89] Hidetoshi Katori. “Longitudinal Ramsey spectroscopy of atoms for continuous operation of optical clocks”. In: *Applied Physics Express* 14.7 (July 2021), p. 072006.

[90] J. Dalibard and C. Cohen-Tannoudji. “Laser cooling below the Doppler limit by polarization gradients: simple theoretical models”. In: *J. Opt. Soc. Am. B* 6.11 (Nov. 1989), pp. 2023–2045.

[91] D V Brazhnikov et al. “Deep laser cooling of magnesium atoms using a 33P2→33D3 dipole transition”. In: *Laser Physics* 24.7 (May 2014), p. 074011.

[92] O. N. Prudnikov et al. “Quantum treatment of two-stage sub-Doppler laser cooling of magnesium atoms”. In: *Phys. Rev. A* 92 (6 Dec. 2015), p. 063413.

[93] E. Kalganova et al. “Two-temperature momentum distribution in a thulium magneto-optical trap”. In: *Phys. Rev. A* 96 (3 Sept. 2017), p. 033418.